Habitable Planet, 2026, 2(1), 234–267

Scilight

Habitable Planet

Journal Homepage: https://www.sciltp.com/journals/hp

Review

The Geology of Hypervelocity Collisions

Sachana Sathyan[1], Sadeeda Marjan[1], Arya Nandakumar[1], Shefana Mahin[1], V. R. Rani[1,2], Sangeeth Sundaresan[1], Praseetha Sugathan[1,3], S. James[4], J. Aswathi[1], Saranya R. Chandran[5], S. Keerthy[6], G. K. Indu[7], V. Aneeshkumar[2], and K. S. Sajinkumar[1,8,*]

[1] Department of Geology, University of Kerala, Thiruvananthapuram 695581, India
[2] Central Ground Water Board, Kerala Region, Thiruvananthapuram 695004, India
[3] Geological Survey of India, Kolkata 700011, India
[4] Department of Earth and Planetary Science, University of Tokyo, Tokyo 113-0033, Japan
[5] National Atlas and Thematic Mapping Organisation (NATMO), Kolkata 700091, India
[6] Department of Geology, School of Environmental Sciences, Mahatma Gandhi University, Kottayam 686560, India
[7] Department of Geology, University College, Thiruvananthapuram 695034, India
[8] Department of Geological and Mining Engineering and Sciences, Michigan Technological University, Houghton, MI 49931, USA
[*] Correspondence: sajinks@keralauniversity.ac.in

ABSTRACT

Hypervelocity impact cratering remains one of the fundamental geological processes that has profoundly shaped planetary surfaces and influenced the structural, chemical, and biological evolution of Earth and other bodies in the Solar System. Impacts by asteroids and comets at velocities of several tens of kilometres per second generate extreme pressures and temperatures, producing diagnostic shock-metamorphic features and lithologies, often unattainable through any other geological processes. This review synthesizes our current understanding of the geology of terrestrial hypervelocity collisions, including impact mechanics, crater-forming stages, morphological classification, diagnostic field and petrographic criteria, mineralogical transformations, and geochemical signatures for impact recognition. The sequential stages of crater formation: contact and compression, excavation, modification, and post-impact geological evolution are explained, with emphasis on simple, complex, peak-ring, and multi-ring craters. The global inventory and uneven distribution of confirmed terrestrial impact structures are evaluated in the context of preservation bias imposed by Earth's active geological processes. Unequivocal indicators of impact origin, including shatter cones, impactites, planar deformation features (PDFs), high-pressure mineral polymorphs, and meteoritic geochemical signatures such as platinum group elements (PGE) and isotopic systems, are examined in detail. The broader geological and planetary implications of impact events are also discussed, encompassing large-scale crustal modification, hydrothermal system development, environmental perturbations, mass extinctions, and the potential of early-life habitability. By integrating geological, mineralogical, geochemical, and planetary perspectives, this review underscores impact cratering as a fundamental planetary process and impact craters as a powerful natural laboratory for understanding extreme conditions and the evolution of Earth and other planetary bodies.

ARTICLE INFO

History:

Received: 25 January 2026
Revised: 20 February 2026
Accepted: 08 March 2026
Published: 16 March 2026

Keywords:

impact crater;
hypervelocity impact;
high-pressure polymorphs;
shock metamorphism

Citation:

Sathyan, S.; Marjan, S.; Nandakumar, A.; et al. The Geology of Hypervelocity Collisions. *Habitable Planet* **2026**, *2*(1), 234–267. https://doi.org/10.63335/j.hp.2026.0037

Research Highlights

- Comprehensive review of geological processes in terrestrial impact craters.
- Crater morphology reflects impact energy and target properties.
- Earth's active geology causes a strong bias in crater preservation.
- Impact craters record crustal, environmental, and biological change.
- Impacts shape regolith, satellites, and surface chronologies at planetary scales.

1. Introduction

Impact cratering is one of the most fundamental geological processes that has shaped planetary surfaces throughout the Solar System, since the accretion of solid bodies more than 4.5 billion years ago [1–3]. Hypervelocity impacts involving asteroids, comets, and meteoroids, typically occurring at velocities of ∼11–72 km s^{-1} [4], release immense kinetic energy over extremely short timescales, producing intense pressures and temperatures that result in fracturing, melting, and vaporization of both target rocks and impactor [1, 5]. These events have exerted a profound influence on planetary evolution, contributing to crustal modification, atmospheric perturbations, mass extinctions, and the delivery and redistribution of volatile components essential to habitability [6].

Terrestrial impact craters, the primary focus of this review, are geological structures formed by hypervelocity collisions on Earth's surface. Although they may superficially resemble volcanic calderas, tectonic basins, or karst features, their origin is fundamentally distinct from endogenic geological processes. Impact craters are uniquely characterized by extreme shock pressures and deformation mechanisms that cannot be produced by volcanism, tectonism, or other internal Earth processes [2]. Consequently, their reliable identification requires a multidisciplinary approach that integrates morphological observations with structural, petrographic, mineralogical, and geochemical evidence, rather than relying solely on surface expression [2, 7].

Recognition of impact cratering as a primary geological process emerged only in the mid-20th century. Prior to this, most circular structures on Earth were interpreted within volcanic or tectonic frameworks [2]. This understanding developed through early investigations of Meteor Crater, Arizona, most notably by Barringer [8], and was later strengthened by the work of Dietz [9] and Shoemaker [10], who established diagnostic criteria for impact crater recognition based on shock-metamorphic features and crater morphology. Since then, impact cratering research has evolved into a strongly interdisciplinary field, integrating geology, geophysics, petrology, mineral physics, geochemistry, planetary science, and astrobiology.

A persistent challenge in the study of terrestrial impact craters is the dynamic nature of Earth's surface and interior. Earth's impact record is continually modified by erosion, sedimentation, metamorphism, and tectonic deformation, leading to significant biases in preservation and detection. Many impact craters are therefore deeply eroded, buried, or tectonically overprinted, and some remain classified only as suspected impact structures [11]. This necessitates an emphasis on precise identification of diagnostic shock-related petrographic, mineralogical, and geochemical signatures, as well as careful consideration of post-impact degradation processes when interpreting crater inventories and formation histories.

Beyond their importance as records of catastrophic events, impact craters serve as unique natural laboratories for investigating processes that operate under extreme physical and chemical conditions. They preserve evidence of extraterrestrial materials and primitive Solar System composition through meteoritic fragments and distinctive geochemical signatures. In addition, they host impact-generated hydrothermal systems and influence crustal evolution and mineralization [12, 13]. At larger scales, impact events have been linked to global environmental change, including atmospheric modification [14], climate perturbations, biological turnover [5], and mass extinctions [6], and have been proposed as potential contributors to processes such as plate tectonics initiation [15] and the origin and early evolution of life.

This review examines terrestrial impact craters using a multidisciplinary framework that integrates geological, geochemical, geophysical, and planetary perspectives to evaluate the role of hypervelocity impacts in shaping Earth's surface, interior, and environmental history. This review highlights impact cratering as a fundamental planetary process that has contributed to crustal modification, environmental change, and biological evolution, while also providing important constraints on impact processes operating across the Solar System.

2. Stages of Impact Crater Formation

The enormous kinetic energy (∼8.3×10^{13} J) of the impactor is transferred to the target within fractions of a second, generating intense shock waves that propagate outward from the point of impact [2]. These shock waves produce transient pressures reaching ∼10–100 GPa, far exceeding the stress levels associated with normal elastic or plastic deformation in terrestrial rocks. This results in unique, permanent shock-metamorphic effects that do not occur in conventional geological environments [2]. Although crater formation is a continuous process, it is divided into three sequential stages [2] (Figure 1).

2.1. Contact and Compression Stage

The contact and compression stage begins when the projectile contacts the target surface. During this phase, typically lasting less than a second, the projectile penetrates a short distance into the target (less than 1–2 times its diameter) before being completely decelerated [2]. At the projectile–target interface, intense shock waves are generated and transmitted outward into the target rocks, while a complementary shock wave propagates backward into the projectile. As these shock waves expand, their pressures decrease rapidly with distance from the impact point due to geometric spreading and energy loss through heating, deformation, and the acceleration of the target rocks [2]. Peak shock pressures near the impact point may exceed 100 GPa, resulting in complete melting or vaporization of both projectile and target rocks. In contrast, pressures decrease outward to levels that produce distinctive shock-deformation features without melting. Beyond that, the shock waves attenuate into low-pressure seismic waves that can fracture rocks but do not produce diagnostic shock metamorphism [2].

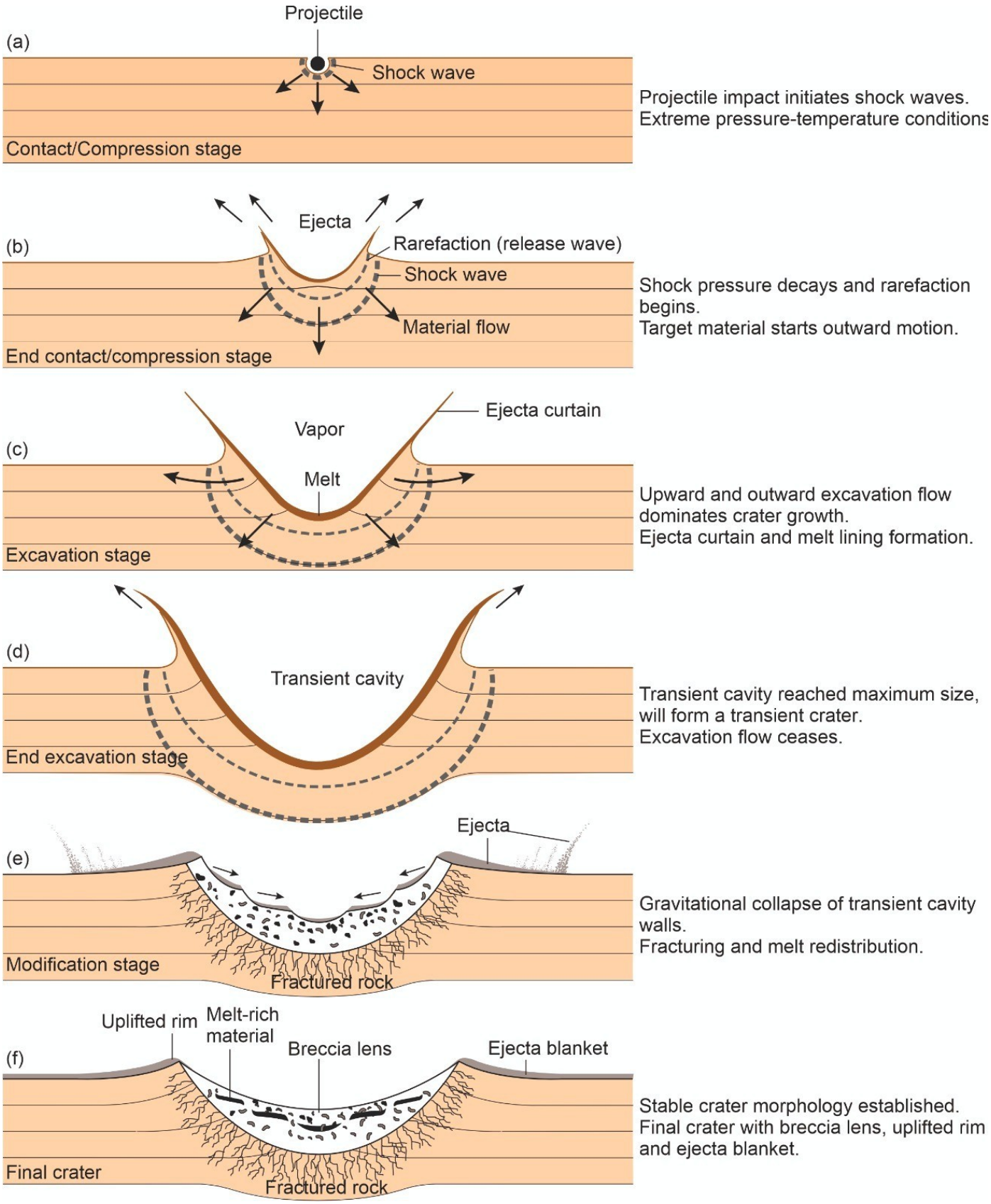

Figure 1. Stages of impact crater formation. (**a**) Contact and compression stage (**b**) End of compression stage (**c**) Excavation stage (**d**) End excavation stage with formation of a transient cavity (**e**) Modification stage (**f**) Final crater structure with an uplifted rim (*Modified after* French [2], Reproduced with permission).

The end of the contact and compression stage is marked by the arrival of release waves that decompress both the projectile and the target. This rapid unloading leads to the near-complete melting and vaporization of the projectile, which thereafter plays no further role in crater formation. From this point onward, crater development is driven entirely by shock-induced motion within the target rocks [2]. For the majority of impacts, the entire contact and compression stage lasts <1 s [2].

2.2. Excavation Stage and Formation of the Transient Crater

The excavation stage follows immediately and involves the outward acceleration of target material by the expanding shock and release waves. During this phase, which lasts from a few seconds for small craters to less than two minutes for immense structures, a bowl-shaped cavity, known as the transient crater, is excavated [2]. Material near the surface is accelerated upward and outward at high velocities, forming an ejecta curtain and depositing fragmented debris beyond the crater rim. In contrast, deeper material is displaced downward and outward more coherently. This excavation produces a transient cavity whose diameter is typically 20–30 times that of the projectile [2]. The transient crater is approximately hemispherical, with a maximum depth of roughly one-third its diameter, a proportion that remains broadly consistent across a wide range of crater sizes. The excavation continues until the shock and release waves lose energy to displace target materials. At this point, the transient crater reaches its maximum size, marking the end of the excavation stage and the immediate onset of gravitational modification [2].

2.3. Modification Stage-Final crater

The modification stage is the third and last stage, and is primarily governed by gravity and rock mechanics, rather than shock processes. Over-steepened walls of the transient crater become unstable and collapse inward; meanwhile, the uplifted material may rebound toward the crater center, particularly in larger craters [2], forming the final crater. In simple craters, this results in a relatively shallow, bowl-shaped final morphology, partially infilled by breccias and impact melt. In larger, complex craters, modification leads to the formation of central uplifts, terraced walls, and peak rings. The most intense modification occurs rapidly, typically within minutes of impact. However, longer-term processes such as isostatic adjustment, erosion, sedimentation, and tectonic overprinting continue to modify crater morphology over geological timescales [2].

2.4. Present-day Crater

The present-day crater reflects its current morphology. During this stage, the original impact structure is further shaped and altered by surface processes, including weathering, erosion, sediment infilling, and tectonic movements. The present-day crater may be partially buried, eroded, or deformed compared to its original form, and its current geomorphic features, such as rim height, depth, and central uplift, reflect the cumulative effects of subsequent geological processes. The current crater is crucial for understanding its long-term evolution and for interpreting the current morphology in the context of planetary geology. One such example is shown in Figure 2, where the pristine final crater morphology of Catota (Mars) is shown, and the present-day crater is Lonar. The long-term changes are evident in Lonar when comparing these two craters. The larger diameter of Lonar reflects the effects of gravitational wall collapse, outward extension of crater rims, and long-term surface modification processes, which progressively alter the original crater morphology [16].

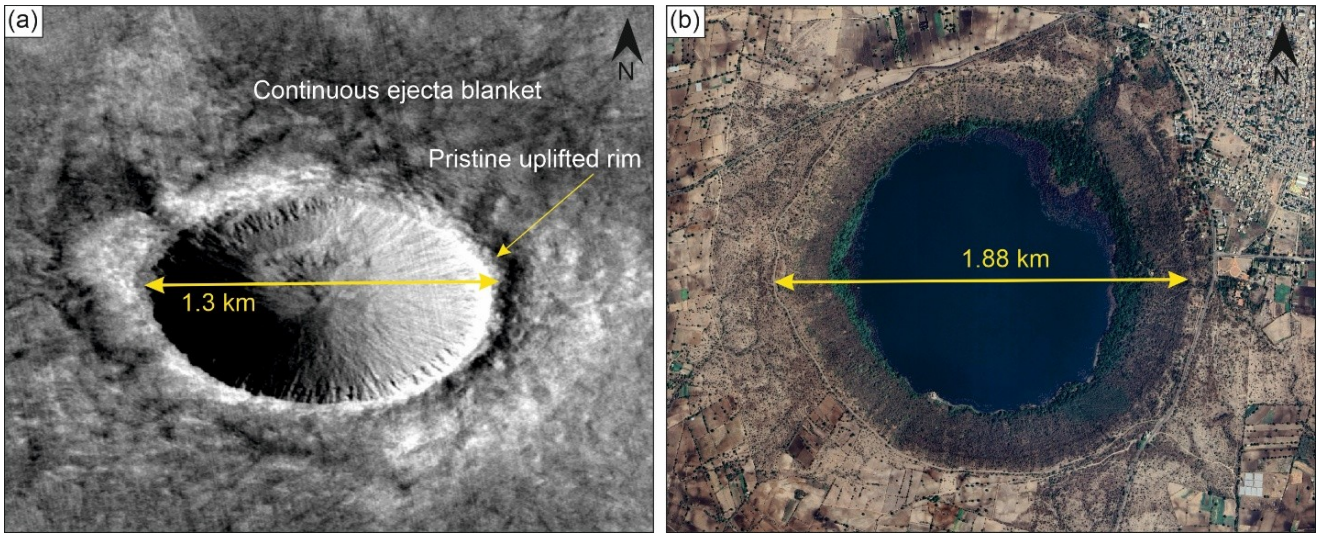

Figure 2. (**a**) Final Crater morphology of Catota (Mars; 1.3 km diameter) (*Source*: JMARS) (**b**) Lonar crater, India, showing the present-day morphology (1.88 km diameter) (*Source*: Google Earth).

3. Classification of Impact Craters

The structure of an impact crater varies systematically with crater diameter, surface gravity, target lithology, and rheological properties [17]. Based on size and structural complexity, impact craters are commonly classified into four morphological types: simple craters, complex craters, peak-ring craters/basins, and multi-ring basins (Figure 3). These classes represent a progression in the degree of gravitational collapse and structural modification of the transient cavity during crater formation.

In minor impacts (Figure 3a), modification is dominated by localized slumping of the crater walls and limited inward collapse, so the morphology of the final simple crater remains similar to that of the transient cavity, leading to the formation of simple craters [1]. Thus, simple craters (e.g., Linné and Lichtenberg B craters on the Moon) are typically bowl-shaped depressions with raised rims and relatively uncomplicated internal architecture. They possess depth-to-diameter ratios of approximately 1:5 to 1:7 and lack central uplifts or terraces due to limited structural collapse following excavation [1, 2, 17].

With increasing crater size, the internal architecture becomes progressively more complex (Figure 3b). Thus, the second type, called complex craters (e.g., Aristillus and Copernicus craters on the Moon), display diagnostic features including a central uplift, a comparatively flat crater floor, concentric faulting, and terracing of the crater walls due to the large-scale gravitational collapse and structural modification of the transient cavity [2]. On Earth, the transition from simple to complex morphology occurs at diameters of approximately 2–4 km in sedimentary rocks and ∼4 km in massive crystalline rocks, whereas on the Moon the equivalent transition occurs at ∼15–25 km, highlighting the inverse relationship with planetary gravity [1–23]. The formation of the central uplift is associated with the rapid rebound and uplift of deep-seated basement rocks beneath the transient crater's center. Simultaneously, rocks around the crater's periphery subside and collapse inward along concentric normal faults, producing ring grabens and terraces. Although the detailed mechanics are still debated, both field observations and numerical models indicate that these large-scale vertical and lateral displacements occur within a few minutes, even for impact structures exceeding 100–200 km in diameter [1].

As crater size increases further, central uplifts become progressively more complex and evolve into central-peak basins and peak-ring basins (e.g., Schrödinger and Apollo basins on the Moon), in which the single central peak collapses outward to form an annular ring of uplifted rocks (Figure 3c). These transitions are most clearly documented on Moon and Mercury, where ancient crater morphologies are well preserved and the critical diameters at which each class forms are larger than on Earth due to lower gravity. On the Moon, peak-ring basins typically develop at diameters of ∼150–200 km, whereas on Earth they occur at ∼20–25 km, as exemplified by the West Clearwater structure [1, 18].

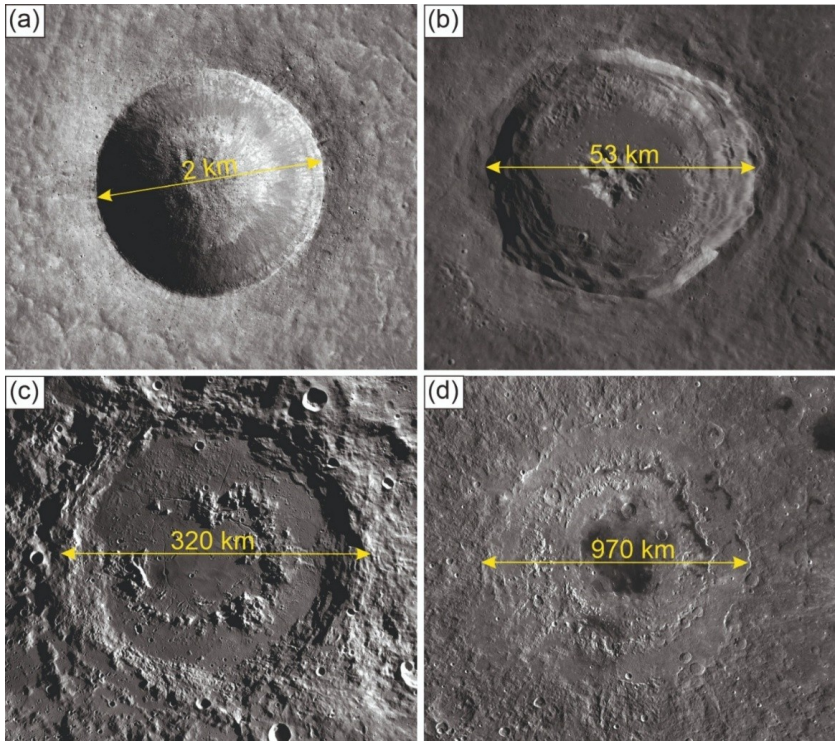

Figure 3. Examples of different types of craters (**a**) Linne simple crater with a diameter of 2 km (**b**) Aristillus complex crater (53 km diameter) with a notable central elevated area (**c**) Schrodinger peak ring basin of 320 km diameter (**d**) Orientale multi ring basin with a diameter of 970 km (all are lunar craters) (Image: Lunar Reconnaissance Orbiter Camera Wide Angle Camera).

The largest impact structures manifest as multi-ring basins, which comprise multiple concentric structural rings separated by down-faulted valleys and may exceed 1000 km in diameter (Figure 3d). These basins formed predominantly during the early heavy bombardment phase of the Solar System and are well preserved on bodies such as the Moon, Mercury, Callisto, and parts of Mars [2]. Examples include Mare Orientale on the Moon (∼900 km) and Valhalla on Jupiter's icy moon Callisto (∼4000 km). On the Moon, the transition to multi-ring basins occurs at ∼200–600 km, implying a threshold of ∼100 km on Earth when scaled for higher gravity [2]. However, terrestrial examples remain uncertain due to deep erosion, and the strongest current candidate for a terrestrial multi-ring structure is Chicxulub, which, although buried, appears well preserved [2]. The formation of multi-ring basins likely involves complex interactions between transient cavity formation, melt production, isostatic uplift, and lithospheric flexure, providing fundamental constraints on early solar system bombardment histories and the mechanical behavior of larger volumes of planetary crusts [19].

4. Components of an Impact Crater

Impact craters display a suite of diagnostic geomorphic features produced during excavation and modification of the transient cavity (Figure 4) [1, 2]. The key geomorphic elements of impact craters include the crater floor, central peak or central uplift, crater walls, elevated rim, ejecta blanket, and, in some cases, ray systems (Figure 4a). The crater floor represents the lowest structural level of the impact depression and commonly preserves materials emplaced during the late stages of crater modification, including impact melt, breccia lenses, and fallback debris [1]. The crater floor may be either bowl-shaped, as in simple craters (Figure 4b,c), or relatively flat in complex structures [17]. Simple impact craters commonly contain a breccia lens on the crater floor, formed by the accumulation of material from the crater wall and comprising a heterogeneous mixture of fragmented, shocked, and locally melted target rocks [1, 20]. In craters with large diameters (tens of kilometres), a central peak or central elevated area develops as the transient cavity collapses and uplifted material rebounds towards the surface, forming a structural high within the crater interior [1]. The crater walls comprise the steep interior slopes connecting the rim to the floor; gravitational slumping during the modification stage commonly generates terrace-like step features [17]. The elevated rim delineates the crater's periphery and is composed of the uplifted, overturned target material formed during excavation [1, 2]. Beyond this rim lies the ejecta deposit, which comprises rock fragments and basement material expelled during the impact, forming a radially thinning, outward-extending blanket around the structure [1, 5]. In numerous fresh craters, particularly those on the Moon, bright ray systems composed of higher-albedo ejecta extend significant distances from the rim; those are called rayed craters [21]. Not all of these geomorphic elements are preserved in terrestrial impact structures. The morphological characteristics of each terrestrial crater undergo continuous evolution post-formation, with factors such as age, plate tectonics, lithology, and climate significantly influencing the rate and manner of denudation-driven modification [2].

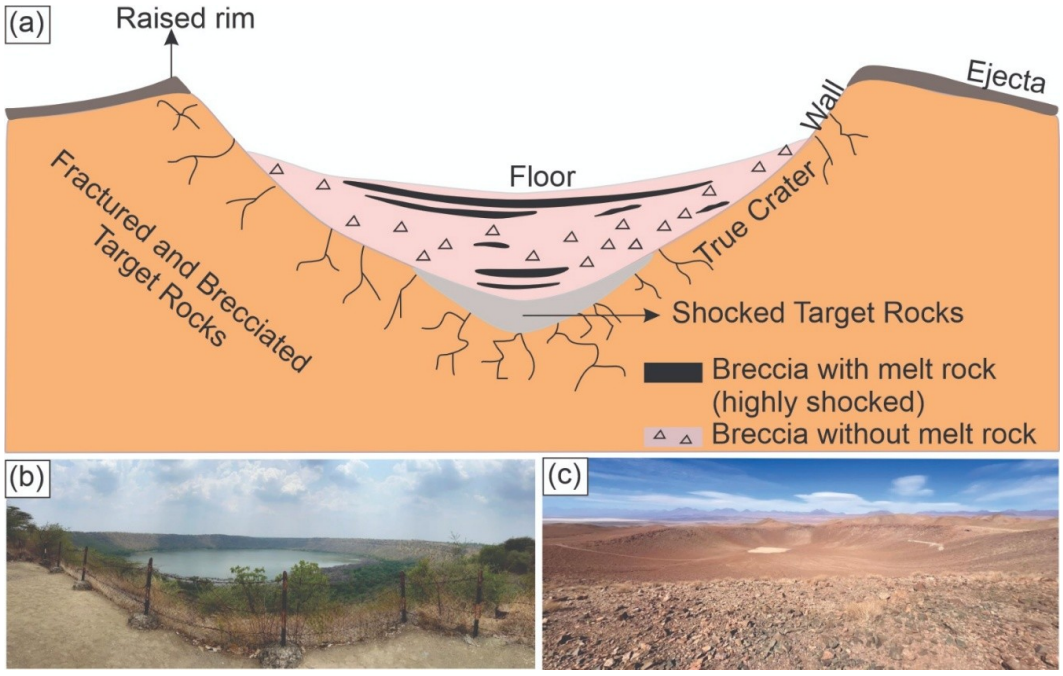

Figure 4. (**a**) Schematic sketch of a simple crater showing the different morphological features (**b**,**c**) Lonar and Monturaqui craters, respectively, which are examples of simple craters. While the central part of Lonar in the basaltic terrain is filled with water, Monturaqui has evaporite deposits, making both suitable candidates for Martian analog studies.

5. Global Inventory

As a result of Earth's active geology, only a small fraction of the impact structures that formed throughout its history are preserved today [22]. Based on recent compilations, ∼211 terrestrial impact craters are confirmed worldwide, supported by geological, geochemical, and geophysical evidence [22–24] (Figure 5; Supplementary Material Table S1). This inventory represents the lowest estimate of Earth's impact record and will continue to uptick as new craters are discovered.

5.1. Global Distribution and Characteristics of Confirmed Impact Craters

The number of confirmed terrestrial impact craters has increased steadily over recent decades, driven by advances in satellite remote sensing, digital elevation models, geophysical imaging, drilling programs, and shock-petrographic techniques [22]. Nevertheless, the preserved crater population remains strongly affected by preservation bias related to Earth's active geology [2].

However, the spatial distribution of confirmed terrestrial impact structures is uneven, with the majority of the craters being identified in North America, Europe, and Australia, and relatively fewer in Asia, Africa, and South America [22]. Differences in crater populations across continents highlight variations in the intensity and duration of geological exploration and impact-cratering research. North America, Europe, and Australia have long-standing research programs focused on impact structures, along with extensive geological mapping and spaceborne observations, which, in turn, enhance crater discovery rates in these regions [22].

Even though confirmed impact craters are noted across all continents, they span a wide range of diameters, from smaller simple craters <1 km in diameter to large complex and multi-ring basins exceeding 150 km, such as Chicxulub, Vredefort, and Sudbury [22]. Cratonic regions dominated by Archean and early Proterozoic crust provide more favorable conditions for long-term crater preservation than younger, tectonically active terrains, resulting in a concentration of known impact structures in stable continental interiors [22]. Stratigraphically, the ages of confirmed terrestrial impact craters range from the Quaternary to Proterozoic, reflecting both Earth's long-term impact flux and the strong preservation bias favoring younger and larger structures [2, 22]. However, even within stable cratonic regions, many impact structures have experienced substantial erosion or burial, resulting in subdued or non-circular morphologies that complicate crater identification [22]. Morphological analyses indicate that only ∼44% of known terrestrial impact craters retain a clearly recognizable surface expression. In contrast, the remaining structures (∼112 craters) are partially eroded, structurally modified, or completely buried beneath younger sediments [22].

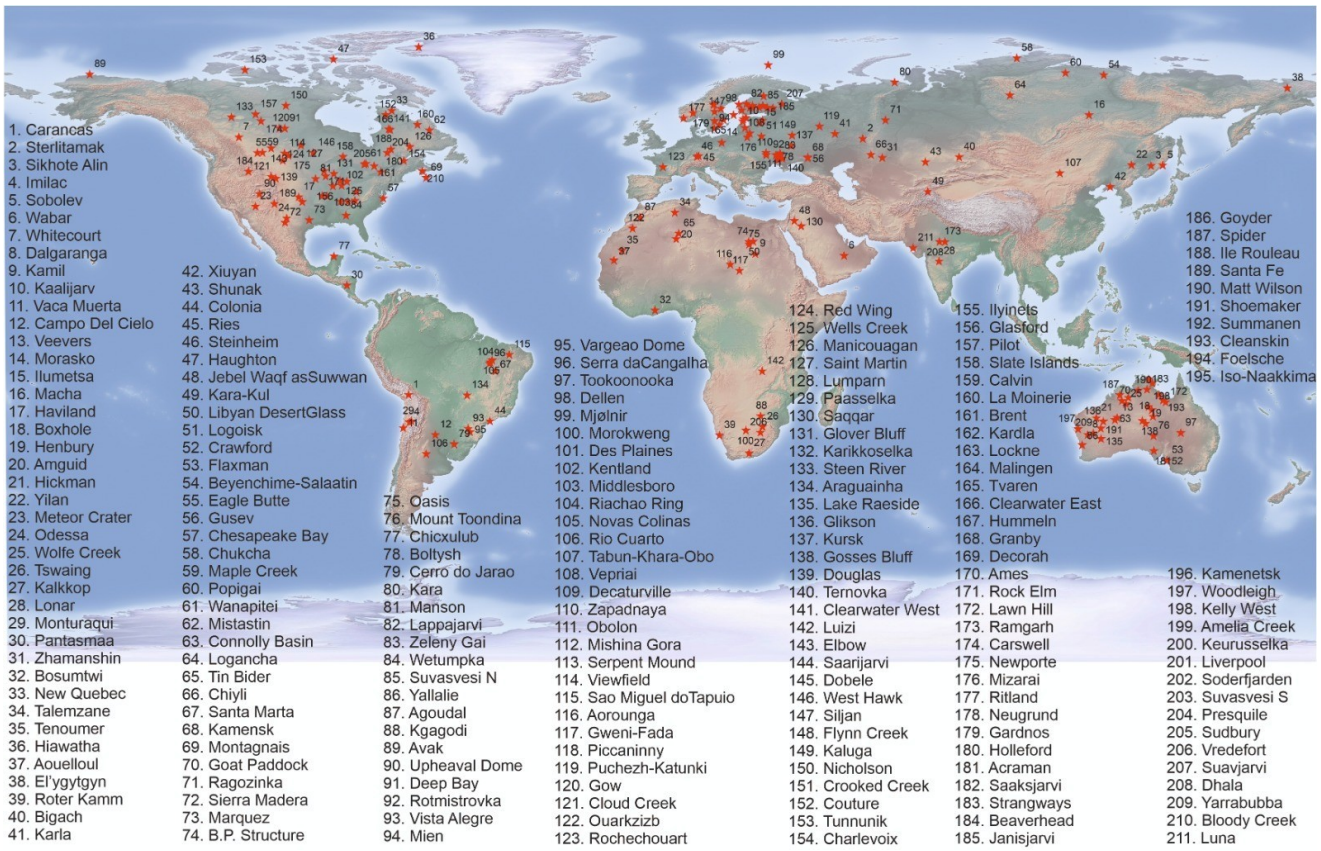

Figure 5. Location of 211 Earth impact craters (Background image: Cross blended Hypso with shaded relief and water (1:10 million Raster Data); Source: https://www.naturalearthdata.com/).

In addition to geological preservation, large areas of the Earth remain underexplored due to dense vegetation cover, sedimentary burial, limited accessibility, or socio-political constraints, particularly in tropical rainforest regions and remote or politically unstable areas [22]. These factors contribute significantly to observational bias in the known crater inventory.

5.2. Suspected Impact Structures

In addition to confirmed terrestrial impact craters, numerous geological structures have been proposed as possible, probable, suspected, or disputed impact sites in global inventories [22]. These structures exhibit some, but not all, of the diagnostic criteria required for confirmation and may lack preserved shock-metamorphic features due to erosion, burial, or post-impact deformation. According to Kenkmann [22], craters including Quarkziz, Yilan, Crawford, Flaxman, Hickman, Piccaninny, Hiawatha, Pantasma, Colonia, and Río Cuarto are regarded as inadequately documented. Additional field investigations, drilling, shock-petrographic analyses, or geochemical studies are needed to establish the origin of their impact beyond doubt.

6. Modern Analytical Framework for Terrestrial Impact Crater Investigation

The investigation of terrestrial impact structures is a multidisciplinary effort that spans a wide range of spatial scales, from planetary remote sensing to nanometer-scale laboratory analysis. The current terrestrial impact research combines remote sensing, geophysics, field geology, petrography, geochemistry, geochronology, shock physics experiments, and finally modelling [25]. No individual tool is unique or diagnostic; rather, robust interpretation requires the convergence of several independent tools.

Within this integrated framework, remote sensing methods serve as the primary tools for initial detection and regional mapping of potential impact structures. Satellite images, aerial photographs, and high-resolution data from planetary orbital remote sensing missions have significantly advanced crater detection and crater density statistics on planetary scales [26]. On Earth, impact structures are preserved to varying degrees, affected by erosion, sedimentation, and tectonics. Impact frequency and the timescales of obliteration indicate the incomplete nature of the terrestrial impact record [25]. Impact structures on Earth cannot be unequivocally identified by remote sensing methods [7]. Geophysical studies have also been particularly useful for investigating structures that have undergone extensive erosion. Gravity and magnetic anomalies have helped identify and characterize several large impact structures, including Chicxulub, Kgagodi, and Morokweng craters [25]. However, gravity and magnetic anomalies can also be produced by features other than impact structures [27].

Field research remains essential for recognizing macroscopic diagnostic indicators such as shatter cones, impact breccias, suevites, and melt rocks. Circular landforms have a large proportion of non-impact origins, including karst, volcanism, tectonics, and glaciations, and must be interpreted with caution. At the microscopic and mineralogical scale, laboratory investigations provide definitive diagnostic evidence. Petrography remains the cornerstone for identifying shock metamorphic features [28]. Where higher resolution is required, scanning electron microscopy (SEM), cathodoluminescence, electron backscatter diffraction (EBSD), transmission electron microscopy (TEM), and Raman spectroscopy are employed to detect planar deformation features, high-pressure polymorphs, and diaplectic glass [25].

Apart from petrography, geochemistry is also important for identifying extraterrestrial components and the nature of the projectile [7]. Common geochemical techniques include X-Ray Fluorescence (XRF), EPMA, Inductively Coupled Plasma Mass Spectrometry (ICP-MS), Laser Ablation Inductively Coupled Plasma Mass Spectrometry (LA-ICP-MS), and Isotope Ratio Mass Spectrometry (IRMS). PGE and chromium isotopic composition are sensitive tracers of meteoritic material [29]. Dating is equally important for linking the impact event with the global stratigraphic markers and events. The techniques include $^{40}Ar/^{39}Ar$ dating, U–Pb dating of zircon, and Optically Stimulated Luminescence (OSL) dating [30]. On the experimental side, the techniques provide quantitative constraints on impact processes. Shock-target experiments help in understanding the pressure-temperature (P–T) conditions necessary for the formation of specific deformation structures [25].

Advances in research on terrestrial impacts come from integrating data, results, experiments, and theories across various spatial and temporal scales. The strength of the research is not in the results of any technique but in the consensus of multiple datasets, which collectively establish the impact origin, the processes of crater formation, and refine the record of impacts on Earth in the context of the rest of the Solar System.

7. Evidence of Impact

We can identify and confirm the origin of terrestrial craters by examining shock-metamorphic effects in minerals and rocks. Shock metamorphic features can be broadly classified into two types: field evidence and petrographic evidence. Field evidence is megascopic (visible to the naked eye), whereas petrographic evidence is microscopic (requiring optical or electron microscopy to observe).

7.1. Field Evidence

7.1.1. Shatter Cones

Shatter cones (Figure 6a) are one of the unequivocal features produced during shock deformation and remain the most reliable macroscopic indicators of impact craters. It forms under lower pressures of 2 to $<$10 GPa [2], and is noted across all three stages of crater formation. Shatter cones rarely occur as standalone entities and are noted in either clusters or with subcurvilinear jointing,

with lengths ranging from millimeters to meters. In a cluster of shatter cones, the cones are found at different orientations from the pre-impact bedding orientations [24], owing to the robust expansion of shock waves radially. These are slightly curved, with radiating striations (horse-tailing) that typically form partial to complete cones, and are usually found in and around the central uplifts of complex impact structures [2] or as part of crater-fill deposits [24]. Shatter cones also occur farther from the crater center as proximal ejecta deposits (which are more susceptible to weathering and erosion). Shatter cones can develop in all rock types; however, they are well developed in fine-grained rocks, such as carbonates and dolomites, and are cruder, with larger striations, in coarser rocks [7]. Shatter cones are difficult to identify and differentiate from non-impact deformational features such as slicken slides (which have friction features on flat planes), wind abrasion structures (which can mimic the conical shape), and cone-in-cone structures (which look similar). With careful observation, shatter cones can be distinguished from similar features by their uniquely oriented apices, which typically point in one direction, and their generally parallel arrangement, indicating a shared origin from a shockwave. Additionally, these striations are pervasive. The parallelism of the axes supports the statement that cone apices point in the direction from which the shock wave originated [7].

7.1.2. Impactites

Impactites are the term used for all rocks produced or affected by a hypervelocity impact event, and they provide valuable information about the impact process [2]. These rocks can be broadly classified as impact breccias (Figure 6b), impact melt rocks (Figure 6c), and suevites (Figure 6d). Impact breccias are formed owing to the fragmentation and re-assembly of rocks during the impact process, and they often contain clasts of shocked and unshocked rocks. They are clastic rocks composed of fragmented and shattered rock material, often mixed with a matrix of fine-grained material [2]. These breccias can contain a wide range of clast sizes and types, indicating the lithological diversity of the target rocks they impact. In contrast, impact melt rocks form from the rapid cooling and solidification of melt generated by the impact, resulting in a more homogeneous texture [1]. Impact melt rocks can be compositionally similar to the target rocks, but may contain inclusions of unmelted clasts or vesicles formed by gas bubbles [2]. The formation of impact melt rocks requires higher temperatures and pressures than those required for breccia formation, typically exceeding 1500 °C and 50 GPa [1]. Suevite is a type of impact breccia that contains a mixture of melt and clastic material, often displaying a characteristic melted texture. These are often found in the central part of impact craters and can provide valuable information about the impact process.

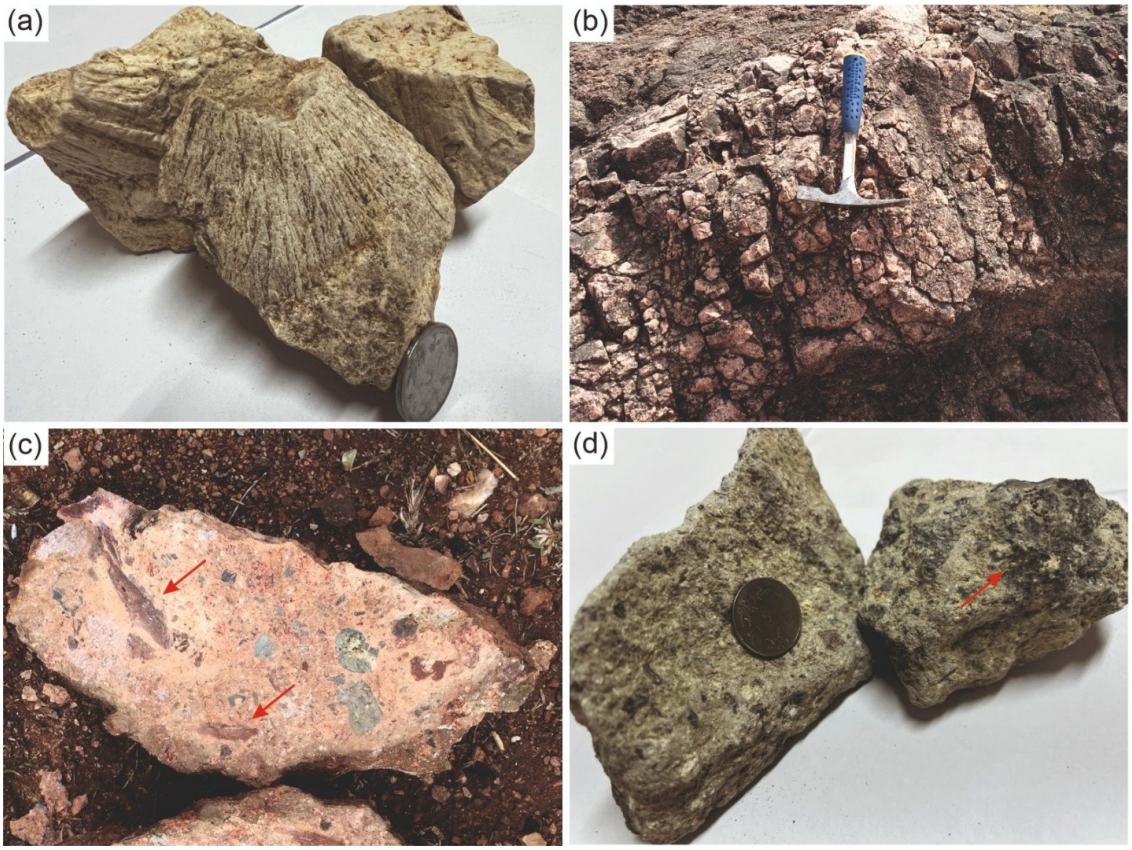

Figure 6. (**a**) Shatter cones for Ries Crater, Germany (**b**) Brecciated granite, Dhala Crater, India (**c**) Melt rock from Dhala (**d**) Suevite from Ries.

7.2. Petrographic Evidence

The study of impactites through petrographic analysis provides the most reliable evidence of impact, revealing a range of distinctive shock-metamorphic features characteristic of impact cratering. The petrographic evidence includes:

7.2.1. Planar Deformation Features

Planar Deformation features (PDFs) are microscopic shock-induced planar lamellae that develop within minerals, particularly quartz, as a result of the passage of high-pressure shock waves (10–35 GPa) generated during hypervelocity impacts [2]. PDFs are commonly observed in quartz, where they are narrow, parallel sets of lamellae oriented along specific crystallographic directions. Usually, multiple sets of planes aligned at specific crystallographic orientations (c(0001), $\omega\{101^-3\}$, $\pi\{101^-2\}$; [7]) cut each other (resembling a hatched pattern). These orientations can be studied by using standard universal-stage or spindle-stage techniques to measure the angle between the quartz c-axes and the PDF plane poles. Then, these angles can be plotted as a histogram to produce a statistical distribution [7]. It is important to measure a sufficient number of PDFs from each sample (e.g., 20–50 grains per thin section). Focus on grains that have at least two PDF orientations. These statistical measurements are the most effective methods for distinguishing PDFs formed by impact from those from other non-impact deformations [7]. Transmission electron microscopy studies demonstrate that PDFs represent zones of intense shock damage, with amorphous silica, high dislocation densities, or closely spaced defect lamellae formed during rapid compression. PDFs are unique, multiple, parallel, thin, closely spaced planes of deformation, and most remarkably, the PDF set(s) remain within a single grain without crossing the grain boundaries, with the individual PDF planes being $\leq$1 µm thick and a few micrometers apart [7]. The mechanism involves the propagation of shock waves that generate extremely high strain rates ($>10^6$ s^{-1}), leading to displacive breakdown of the quartz structure along rational crystallographic orientations [2]. Experimental shock-recovery studies confirm that PDFs form during the compressive stage of shock loading and are preserved upon rapid pressure release, distinguishing them from tectonic deformation features [31]. PDFs appear remarkably straight, sharp, and continuous under the optical microscope; they occur in a few rhombohedral planes $\{101^-$ n$\}$, with $=$ 3 (ω type) and 2 (π type) as the most frequent values; $n = 1$, 4 and $n = \infty$ (i.e., basal plane) are also detected [32]. The presence of PDF in the target rocks has been widely accepted for confirming the impact origin. In addition to quartz, PDFs can form in minerals such as feldspars, garnet, sillimanite, and zircons [33]. Even though PDFs are developed in other minerals, the identification of impact structures mainly hinge on PDFs present in quartz, owing to several reasons such as (i) quartz being abundant in most target rocks [7], (ii) Quartz can be used as a 'shock barometer' because the formation of Planar Deformation Features (PDFs) in quartz is directly related to the pressure it experiences during an impact event, and (iii) quartz being the most stable mineral to preserve PDFs even if the mineral undergoes metamorphism, erosion and sedimentation [7].

7.2.2. Planar Fractures (PF) and Feather Features (FF)

Planar fractures (PF) are a type of shock metamorphic feature commonly observed in quartz grains. Compared to PDFs, PFs can develop at lower shock pressures ($<$10 GPa). This type of fracture is characterized by sets of parallel, planar cracks that form during the propagation of a shock wave. The multiple sets of PFs seen in quartz appear similar to cleavage, i.e., 2–3 sets per grain. PDFs differ from PFs since PFs are relatively thicker than PDFs and are widely spaced (from $>$200 to 100–500 µm apart) [7]. Feather features (FF) are shear-induced, narrowly spaced (1–10 µm) subparallel-parallel lamellae ($\sim$10–100 µm) branching off a PF [24]. PDFs, PFs, and FFs are important microdeformation features observed in crater-fill deposits, ejecta, crater floors, and *in-situ* target rocks [24].

7.2.3. Ballen Quartz

The most commonly used mineral for identifying meteorite impact structures is quartz, due to its durability and tendency to develop distinctive deformation features [7]. Ballen quartz was first reported from the Mein Impact Structure. Ballen texture is an unusual texture observed in some quartz grains formed during impacts (Figure 7a). These are ovoid to arcuate microstructures that form above $\sim$30 GPa and at annealing temperatures of 1150–1300 °C [34]. Ballens are not cracks or vacuoles but are spheroidal or grape-like bodies that interpenetrate or abut each other, with a size range of 8 to 214 µm [34]. Ballen quartz mainly occurs in diaplectic quartz or in impactites [34]. The mechanism of ballen quartz aggregate formation is still a matter of debate. Current models are largely based on evidence of silica phase transformations, particularly the conversion of lechatelierite or diaplectic glass into cristobalite, followed by its subsequent transformation into alpha quartz. Ferrière et al [35] proposed that ballen formation may occur through two possible genetic processes: (i) an impact-induced solid–solid transformation of α-quartz into diaplectic quartz glass, followed by high-temperature development of ballen composed of β-cristobalite and/or β-quartz, and subsequent back-transformation to α-cristobalite and/or α-quartz; and (ii) a solid–liquid transition from quartz to lechatelierite, followed by high-temperature nucleation and crystal growth. Ballen quartz is classified based on its optical properties and the crystal structure of the SiO_2 constituent of the ballen. Five types of ballen silica were proposed by Ferrière et al [36]: α-cristobalite ballen with homogeneous extinction (type I); α-quartz ballen with homogeneous extinction (type II); α-quartz ballen with heterogeneous

extinction (type III), or with inter-ballen recrystallization (type IV); and chert-like recrystallized ballen α-quartz (type V). In addition, ballen with a toasted appearance was reported from impact structures such as Popigai [37], Wanapitei [38], Dhala [39], Rochechouart, Sääksjärvi, and Ternovka craters [34]. The toasting is due to vesicle formation after pressure release at high post-shock temperatures, and this marks the onset of quartz breakdown due to heating [34]. Ballen quartz can be used as an impact-induced criterion because it is likely the result of the back-transformation from shock-induced states [34].

7.2.4. Diaplectic Glass

Diaplectic glass was first observed in the Ries crater. Diaplectic glasses (Figure 7b) are the transformation of individual minerals to amorphous phases without actual melting [2]. Higher shock pressures (35–45 GPa) transmit more energy into the crystal and convert the crystal into an amorphous (glassy) phase [20]. A mineral that melts into a liquid at temperatures above its melting point is a conventional glass. In contrast, a diaplectic glass does not melt or flow, preserving the original mineral fabric and texture [2]. Diaplectic glasses are a unique criterion for identifying impact structures. Compared to shatter cones and PDFs, diaplectic glasses are less common in impact structures because they form at higher pressures [7]. Diaplectic glasses serve as a key indicator for high levels of shock metamorphism in impact craters [40]. At high shock pressures ($>$30–50 GPa), the tectosilicate minerals (chiefly quartz and feldspar that develop PDF) are converted to amorphous glassy phases without actual melting, known as diaplectic glass [7]. The high pressures induce solid-state transformation of monomineral grains [24]. The absence of flow textures and vesicles can be attributed to a solid-state transformation rather than actual melting. Diaplectic glasses are detected at the crater center (central peak, crater-fill deposits); the point of peak pressures [7]. Figure 8 depicts the different shock features formed in the Dhala impact crater with increasing pressure.

7.3. Geochemistry

Geochemistry is an important tool for confirming the presence of meteorite impact craters and deciphering their evolution. It involves geochemical characterization of target rocks, impactites, and any extraterrestrial components. Additionally, the determination of impactor composition and the assessment of the causes of environmental change are usually done through chemolithostratigraphic analyses [41]. Geochemical analyses also help to identify the presence of extraterrestrial components within impactites. In a meteorite impact event, only a minor fraction (usually $\ll 1\%$) of the meteorite gets mixed with the larger quantity of the target rock [42]. The resulting impactites would have only minor chemical changes. Detecting small amounts of meteoritic material within the normal upper-crustal composition of the target rocks is extremely difficult. Thus, elements having high abundances in meteorites and lower concentrations in terrestrial crustal rocks are of utmost interest in geochemical studies. The existence of different meteorite groups and types (three main groups—stony meteorites, iron meteorites, and stony-iron meteorites) with variable siderophile element compositions is an added complexity in geochemical analysis.

Additionally, mixing calculations can be applied to reconstruct the proportions of different rock types comprising breccias and impact-melt rock after all rock types present at an impact site are identified and analyzed. Indigenous siderophile-element contents in impactites can be determined using such mixing calculations, which are essential for assessing the possible mixing of extraterrestrial components during the impact event [41]. The trace element composition of different rock types can be studied to understand alteration processes imparted by the natural environment or by impact-induced hydrothermal processes. Compositional variations, for example, in volatile elements, will address both physical and chemical processes that occurred during the impact event by evaluating the high-temperature elemental fractionation that prevailed during the impact. Analyses including both major and trace element detection help identify individual minerals in rocks or melt rocks, as well as compositional changes within impact glasses such as tektites. Sampling and sample preparation are crucial to geochemical analyses of impactites. Usual geochemical methods are used to analyze major and trace elements in impact-related rock samples. Some major analytical techniques used in the identification of bulk rock major and trace-element analyses are X-Ray Fluorescence XRF, Inductively Coupled Plasma Atomic Emission Spectrometry (ICP-AES), ICP-MS, Instrumental Neutron Activation Analysis (INAA), and Electron Probe MicroAnalysis (EPMA). Mineral and microscale analyses are carried out using ordinary electron- and ion-beam methods.

7.3.1. Major Elemental Oxides

The major oxide concentrations display significant variability among samples derived from different source lithologies. In contrast, samples collected from the same impact structure exhibit relatively limited compositional dispersion, suggesting a broadly homogeneous composition within individual craters. The major oxide geochemistry of selected target rocks and impactites from several well-studied impact structures—including Aorounga (Chad) [43], Gweni Fada (Chad) [43], Meteor (USA), Brent (Canada) [44], Bosumtwi (Ghana) Gardnos (Norway) [45], Lonar (India) [46], Ramgarh (India), Wanapitei (Canada) [38], and Xiuyan (China) [47], has been evaluated using Harker variation diagrams (Figure 9a–d). Binary plots of SiO_2 against TiO_2, MgO, Fe_2O_3, and Al_2O_3 were constructed to examine compositional trends and source rock characteristics. In Figure 9a, a negative correlation between Al_2O_3 and SiO_2 is evident as SiO_2

increases from 50% to 100%. High-alumina rocks indicate clay-rich or feldspathic (like basaltic) target rocks, whereas points nearing 100% silica are indicative of silica-rich target rocks. Figure 9b, in general, shows a scattered distribution of high TiO_2 content corresponding to lower silica content. In SiO_2 vs. Fe_2O_3 (Figure 9c), a sharp decrease in Fe_2O_3 can be seen as SiO_2 increases. The Lonar melt rock from basaltic target rock shows high Fe_2O_3 content, whereas the samples from Wanapitei are rich in SiO_2, as they are derived from predominantly silicic target rocks. In Figure 9d (SiO_2 vs. MgO), a sharp inverse relationship is evident. The samples from Barringer Crater are distinct, as their high MgO content reflects the presence of dolomitic lithologies within the Kaibab Formation target rocks.

7.3.2. Trace and Rare-Earth Element Analyses

Nickel (Ni), cobalt (Co), copper (Cu), gallium (Ga), germanium (Ge), manganese (Mn), chromium (Cr), and vanadium (V) are the common elements studied. The elevated concentrations of these elements in impact melt rocks and breccias, relative to target abundances, are indicative of possible contributions from a chondritic or an iron meteorite. However, it is difficult to differentiate an achondritic projectile as it has significantly lower contents of these key elements. All target rock samples should also be examined to determine the background concentrations of these elements to understand the extent of projectile mixing. At present, meteoritic components have been detected in only a handful of the ∼211 known terrestrial impact craters.

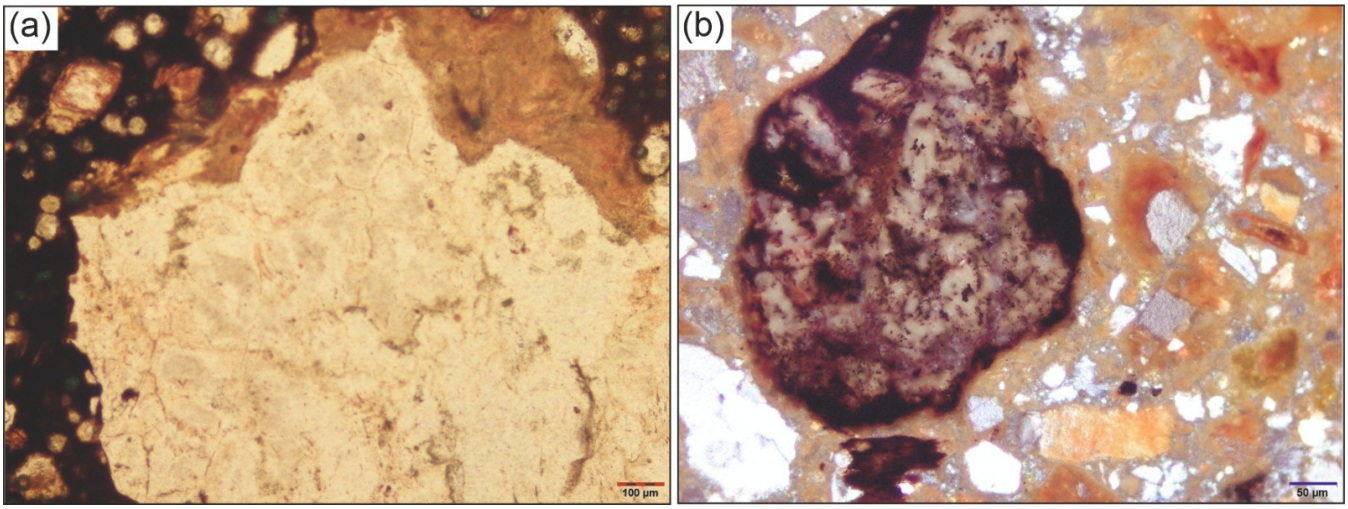

Figure 7. (**a**) Ballen quartz and (**b**) diapletic glass from the impactites of Dhala Crater.

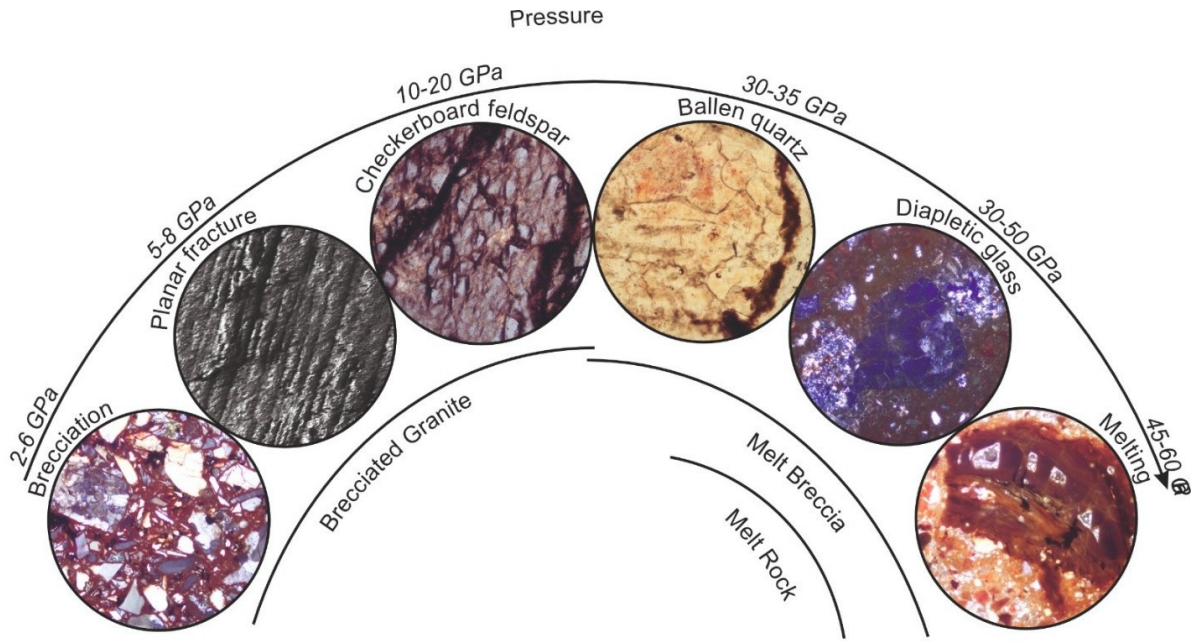

Figure 8. Impact features identified in Dhala impactites with respect to the change in pressure.

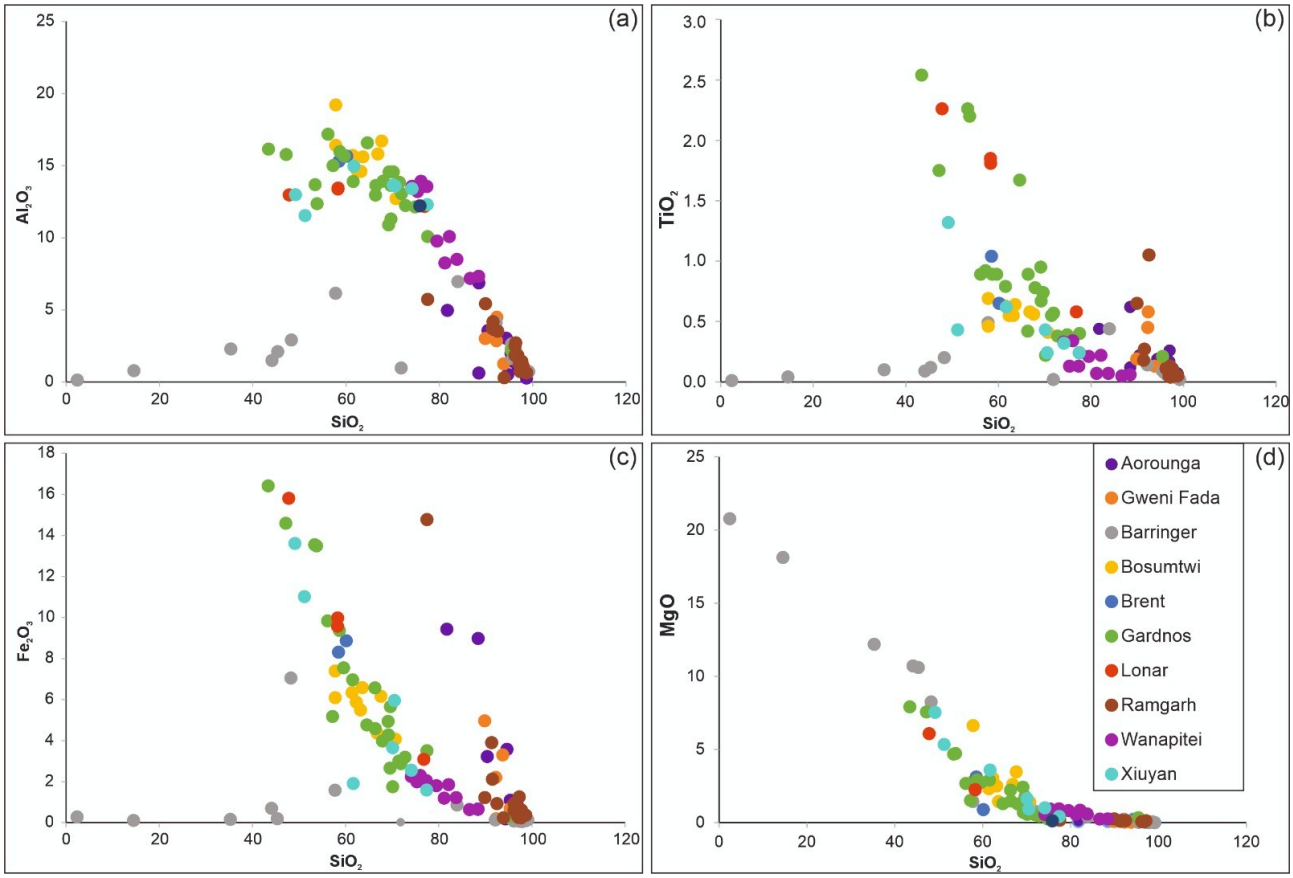

Figure 9. Harker's variation diagram for different impactites (**a**) SiO_2 vs. Al_2O_3 (**b**) SiO_2 vs. TiO_2 (**c**) SiO_2 vs. Fe_2O_3 (**d**) SiO_2 vs. MgO.

Of these elements, the most commonly used elements in the detection of meteoritic components are nickel (Ni), cobalt (Co), and chromium (Cr). The interelement ratio of these elements provides valuable clues to the type of impactor involved. Stony (chondrites) and iron meteorites can be distinguished from each other if the meteorite contribution exceeds 0.01% by weight, since chondrites have high concentrations of Cr (∼0.26 wt%) relative to the variable content noted for iron meteorites (∼100 times less than the concentration in chondrites). It is also reported that iron meteorites have low Ni/Cr or Co/Cr ratios. Hence, the Cr concentration and determination of Ni/Cr or Co/Cr ratios in impactite samples can be used to distinguish between stony (chondrites) and iron impactors [48]. A detailed study of these elements in the target rocks must be conducted to eliminate any confusion before reaching a conclusion. Pure meteoritic abundance ratios can be obtained through mixing calculations, in which the relative proportions of the various target rocks involved in the production of melt rocks or breccias are determined, along with the indigenous elemental concentrations, and subtracted from the concentrations found in impactites [18]. Therefore, it is essential to analyse all rock types that are known or suspected to be present in the target area [41]. Eventually, the interpretation becomes complicated when too many target rocks are involved in the generation of impact melt rocks or breccia, as some lithologies may remain undetermined due to erosion-induced loss and lack of exposure [49].

A chondrite-normalized rare earth element (REE) diagram (after McDonald et al. [50]) was constructed for samples from the Aorounga (Chad), Gweni Fada (Chad), Meteor (USA), Brent (Canada), Gardnos (Norway), Lonar (India), and Ramgarh (India) impact structures (Figure 10a). The REE patterns of most samples display broadly similar fractionation trends and parallel profiles, indicating comparable source characteristics and limited geochemical modification during impact processes. A few samples from the Gardnos crater exhibit noticeable anomalies, marked by localized enrichments and irregular fractionation patterns, which may reflect compositional heterogeneity in the target lithology or variable degrees of impact-induced alteration. Although the overall trends appear broadly similar, a more detailed evaluation of individual profiles reveals additional compositional variability. Overall, the samples show a negative slope from left to right in the signature of the continental crustal rocks. Most of the samples show a negative Eu anomaly indicative of plagioclase fractionation, possibly due to the heating by the impact event. Samples from the Lonar crater show a relatively flat profile, characteristic of basaltic rocks, and are less enriched in LREEs than silicic target rocks.

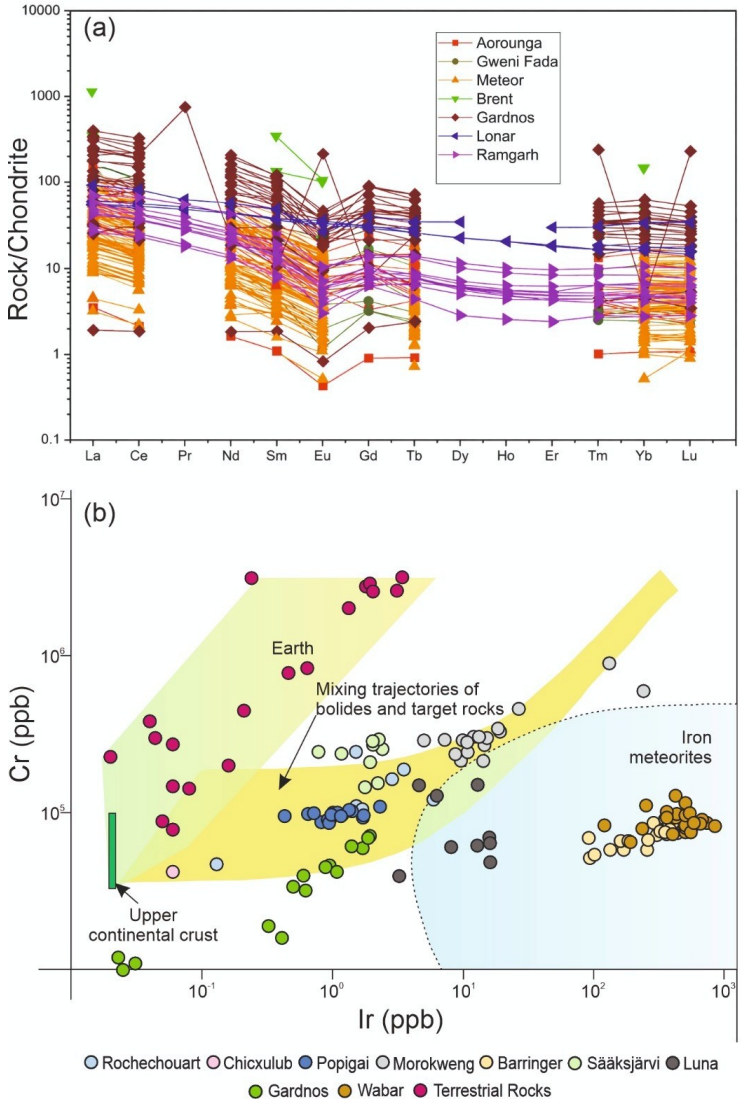

Figure 10. (**a**) Chondrite-normalized rare earth element (REE) diagram (after McDonough and Sun [51]) for Aorounga (Chad), Gweni Fada (Chad), Barringer (USA), Brent (Canada), Gardnos (Norway), Lonar (India), and Ramgarh (India) impact craters (**b**) Ir–Cr plot for different impactites depicting terrestrial and different meteoritic fields.

7.3.3. Platinum Group Elements (PGEs)

PGEs consist of platinum (Pt), palladium (Pd), rhodium (Rh), ruthenium (Ru), iridium (Ir), and osmium (Os). PGEs and gold (Au) are considered better for identifying meteoritic components than Cr, Ni, and Co [48]. In chondrites and most iron meteorites, the abundance of PGEs is several orders of magnitude higher than that in the terrestrial crustal rocks (both continental and oceanic). Chondrites have Ir and Os concentrations in the range of 400–800 ppb [52], whereas continental crustal rocks are reported to have Ir or Os concentrations in the order of 0.02–0.03 ppb. Chondritic meteorites are reported to have average abundances of about 700 ppb Ir, 1800 ppb Pt, 700 ppb Pd, and 900 ppb Ru [52]. On the other hand, even in mantle xenoliths, the PGE abundances are in the order of 2 ppb Ir, 5 ppb Pt, 2 ppb Pd, and 4 ppb Ru. Upper continental crust has concentrations 100 times lower than those of mantle rocks. Iron meteorites show a wider range of these elemental concentrations. Thus, PGEs are reported to have a very high signal-to-background ratio, owing to their low indigenous concentrations and high concentrations in the contaminating meteorites. Ir is the most commonly used PGE to trace the meteoritic content in an impact event, because it can be determined with greater sensitivity and ease than other PGEs. The observed Ir anomaly suggests the potential to detect additional PGEs within a restricted subset of the samples. Alvarez et al. [6] discovered significant enrichment in the concentrations of PGEs, Co, and Ni in the thin clay layer, making the Cretaceous-Paleogene (K-Pg) boundary compared to normal crustal rocks. Alvarez et al. [6] interpreted the notable enrichment (up to four orders of magnitude) and characteristic inter-element ratios as resulting from the impact of a large asteroid or comet that caused the Chicxulub impact event. This exemplifies that geochemistry contributes

significantly to remarkable discoveries. The initial content determination was based on neutron activation analysis, but such measurements are now more commonly performed by ICP-MS. Quantification of PGE content has several limitations due to their low abundances, inhomogeneous distribution in rocks, and detection limits. Figure 10b shows Ir versus Cr for different impactites across the globe (Rochechouart [53], Sääksjärvi [53], Chicxulub [54], Popogai [55], Morokweng [56], Barringer [57], Luna [58], Gardnos [59], Wabar [60]) along with a suite of terrestrial rocks. This plot shows the mixing fields between different meteorite classes and terrestrial rocks. The terrestrial rocks contain low Ir and high Cr concentrations, thereby falling within the 'Earth' field. In contrast, all impactites except Barringer, Wabar, and Luna fall in the mixing fields of chondritic projectiles and terrestrial rocks. This field has low-high Ir and moderate-high Cr concentrations, depicting the different extent of projectile-target mixing. Barringer, Wabar, and Luna plot in the 'iron meteorite' field, indicating the projectile is iron (instead of chondrite). The combination of the Ir–Cr plots with other petrological and geochemical analyses helps establish the impact origin of a structure.

7.3.4. Isotopes

Isotopic studies are essential for identifying and confirming terrestrial impact craters by providing chronological, geochemical, and extraterrestrial source constraints that complement structural and petrographic evidence. Radiometric dating systems such as U–Pb, ^{40}Ar/^{39}Ar, Rb–Sr, and Sm–Nd establish precise ages for impact melt rocks and shocked minerals [18]. For example, high-precision geochronology at the Chicxulub crater confirms its formation at ∼66 Ma, coincident with the Cretaceous–Paleogene boundary [61]. Radiogenic isotope systems such as Sr–Nd–Pb–Hf further constrain the source of impact melts and help distinguish impact-generated melts from mantle-derived igneous intrusions, which was critical in resolving the origin of the Sudbury Basin [62]. Additionally, isotopic tracers of highly siderophile elements, particularly Re–Os systematics, allow the detection of meteoritic components even when macroscopic meteorite fragments are absent, providing a definitive extraterrestrial signature [63]. Non-mass-dependent chromium isotope anomalies (^{54}Cr) further strengthen identification by constraining the type of impactor involved [64]. Oxygen isotope ratios (δ^{18}O) help distinguish impact glasses from volcanic glasses by reflecting differences in source reservoirs and fractionation behavior [7]. Moreover, isotopic homogeneity across large melt sheets, such as those at the Manicouagan crater, supports formation by instantaneous large-scale melting during hypervelocity impact rather than incremental magmatic processes [65]. When integrated with diagnostic impact-shock features, such as PDFs in quartz, shatter cones, and geophysical anomalies, these isotopic tools provide a robust, multidisciplinary framework for the convincing identification of impact structures [7].

Rubidium (Rb) – Strontium (Sr) and Samarium (Sm) – Neodymium (Nd) Isotopes

The classic isotopic systems of Rb–Sr and Sm–Nd are commonly used in meteorite impact studies to determine the ages of impact events, primarily by separating phases from impact melt rock samples and plotting isochron diagrams. The systems of Rb–Sr and Sm–Nd are based on β-decay of ^{87}Rb to ^{87}Sr with a half-life of 48.8 Ga and α-decay of ^{147}Sm to ^{143}Nd with a half-life of ^{106}Ga, respectively. Isotope systems can also be used as tracers for source rocks [41]. Isotopic systematics can differentiate between a crustal source for the crustal rocks and a deep-seated or mantle source for the melt rocks. Melt rocks in young impact structures with comparatively high ^{87}Sr/^{86}Sr values indicate they were derived from the melting of older, more radiogenic continental crustal rocks.

Osmium (Os) Isotopes

The Os content in meteorites is several orders of magnitude higher than that of terrestrial crustal rocks. ^{187}Os isotope is formed by β-decay of ^{187}Re with a half-life of 42.3 $\pm$ 1.3 Ga. In meteorites, Os abundances are more than the Re abundances, with Re/Os ratios being less than or equal to 0.1. In contrast, in terrestrial crustal rocks, the Re/Os ratios are generally no lower than 10. The abundance of the radiogenic isotope ^{187}Os is normalized to the abundance of a non-radiogenic isotope ^{188}Os, as in conventional methods. In old crustal rocks, the ^{187}Os/^{188}Os ratio increases rapidly with time, with an average upper crustal value of ^{187}Os/^{188}Os = 1–1.2, due to the high Re and low Os concentrations in older rocks. For meteorites, the ^{187}Os/^{188}Os ratio is low in the range of ∼0.11–0.18. There are only minor changes in the meteoritic ^{187}Os/^{188}Os ratio with time since Os is more abundant than Re in meteorites. For impact-related materials, the Os isotopic system was first successfully applied in the study of K-Pg boundary clays. However, initial attempts to study the Os isotope composition of impactites were unsuccessful due to their low Os abundances. After the introduction of negative thermal ionization mass spectrometry (NTIMS), the first successful application of the Os isotope system was reported for tektites and impact glasses from the Bosumtwi impact crater in Ghana [66]. The crustal target rocks show a significant Os isotopic signature in the impactites because of the relatively high meteoritic Os abundances [42]. Achondrites have much lower PGE abundances compared to chondritic and iron meteorites; therefore, a much higher meteoritic addition is required to detect their presence. According to Koeberl and Shirey [67], the Os isotope method is the most reliable among the PGE elemental abundances and ratios in terms of detection limit and selectivity. This method has been successfully used to identify meteoritic components in several impact craters and to confirm the impact origin of craters. However, one disadvantage of this method is the inability to detect the projectile type [42].

Chromium (Cr) isotopes

Cr isotopes provide important information for recognizing and identifying extraterrestrial components in impactites [68, 69]. In ideal cases, it helps to distinguish between three groups of meteorites, viz., (i) carbonaceous chondrites, (ii) enstatite chondrites, and (iii) all other types of meteorites. Variations in chromium isotopic composition are determined relative to the terrestrial standard $^{53}Cr/^{52}Cr$ ratio and reported as $\varepsilon^{53}Cr$ values, which represent deviations from this reference composition [70]. Terrestrial and lunar (anorthosite) rocks show little variation in the $^{53}Cr/^{52}Cr$ ratio [68]. For meteorites, $^{53}Cr/^{52}Cr$ ratios vary between +0.1 and +1.3 ε [68]. Carbonaceous chondrites show a ^{53}Cr deficit due to the $^{54}Cr/^{52}Cr$ second-order fractionation correction used, as carbonaceous chondrites contain a presolar ^{54}Cr-rich component [70]. So far, only carbonaceous chondrites and enstatite chondrites have been identified by characteristic Cr-isotopic ratios that differentiate them from other chondrites and differentiated meteorites [69].

7.4. Mineralogy

Due to the high-pressure solid-state transformation, phase transitions in minerals are common during impact events [42]. Some common minerals that undergo phase transitions to form metastable high-pressure phases are: stishovite and coesite from quartz; maskelynite from plagioclase (Figure 11); majorite from pyroxene; reidite from zircon; and ringwoodite from olivine. FRIGN (Former reidite in granular neoblastic) zircon ($\geq$30 GPa, $\geq$1673 °C) [24], a reliable indicator of high-pressure effects, is another example of mineral phase transition. Because zircon and quartz are minerals found across various lithologies, the associated high-pressure phases are more commonly identified in many craters. Coesite, a monoclinic polymorph of quartz, has been found in the Reis and Barringer craters. Stishovite, a tetragonal polymorph of quartz, has also been reported from Ries. Akaogiite, a rare high-pressure polymorph of rutile; albitic jadeite (a high-pressure impact-induced phase of pyroxene), and kokchetavite (a metastable hexagonal K-feldspar polymorph) are other high-pressure forms identified from Ries crater, Germany. Kokchetavite is seen in the alkali-rich melt glasses in suevite, either as a single phase or together with liebermannite and albitic jadeite. Impact-derived diamonds are reported from Popigai (Siberia) and Ries. High-pressure carbon in graphite- or coal-bearing target rocks can form diamonds at impact sites. In Xiuyan, a 1.8 km diameter crater in North China, Maohokite has been discovered in shocked gneiss. Maohokite is a post-spinel polymorph of magnesioferrite $MgFe_2O_4$, a member of the magnetite series of the spinel supergroup.

Additionally, the high temperatures associated with the impact event are demonstrated by high-temperature minerals such as lechatelierite and baddeleyite [42]. Lechatelierite is monomineralic quartz melt formed at temperatures $>$1700 °C, and baddeleyite is a product of thermal decomposition of zircon (temperature of $\sim$1900 °C).

Impact craters also host minerals that are not directly related to shock metamorphism, but are generated later through hydrothermal processes. Dominant secondary mineral assemblages found in all impact craters include clay minerals (smectites, chlorites, and mixed-layered smectite-chlorite), various zeolites, calcite, and pyrite, along with local occurrences of cristobalite, quartz, opal, anhydrite, gypsum, prehnite, epidote, andradite, actinolite, and albite. The hydrothermal mineralogy is generally determined by the composition of the target rocks and the composition, temperature, Eh, and pH of the available solutions [42]. Despite the large number of minerals mentioned here, the association of the minerals with an impact event depends on the broader geological context and setting. All the minerals can be noted in the crater fill deposits, although some minerals can be noted across dykes in the crater floor and ejecta deposits.

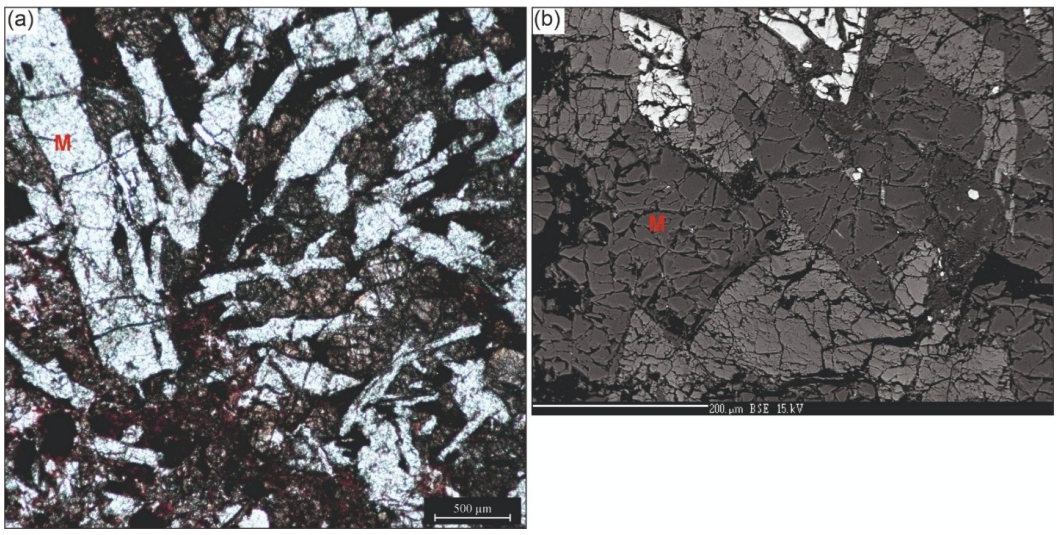

Figure 11. Maskelynite from basalt of Lonar crater (**a**) photomicrograph (plane polarized) (**b**) BSE image of fractured maskelynite (*Photo courtesy*: Dr. Dwijesh Ray).

8. Products of Impact

An impact event initiates a series of smaller-scale events as shock waves propagate, leading to the formation of impact products. The impact system includes both the impact structure and a range of impact resultant products. While the prominent morphology of relatively younger, well-preserved craters (e.g., Lonar, Meteor) can be visually identified on-site, the impact origin of a crater is rarely ascertained without successful identification of multiple impact products. The broad spectrum of impact products can be classified into (i) physical and (ii) chemical products.

8.1. Physical Products

Physical products are physical derivatives of an impact event; i.e., these entities can be observed either directly or using microscopic techniques. The products can be divided into (i) shocked products, (ii) brecciated products, and (iii) other ejected products; broadly following the classification by French and Koeberl [7], and Osinski et al. [24]. Each of these products is explained below:

8.1.1. Shocked Products

Shocked products are produced when the target rocks are subjected to the mechanical effects of expanding shock waves. High-pressure shock waves [2, 7] deform target rocks and minerals to varying degrees, depending on the shock pressure. The shock-deformation products can be either macroscopic (e.g., shatter cones; Figure 6a) or microscopic (e.g., diaplectic glasses (Figure 6d); high-pressure polymorphs (Figure 11); and microdeformation features such as PDF, PF, and FF). The shocked products mostly form during the contact and compression stage of crater formation.

8.1.2. Brecciated Products

The expanding shock wave generates not only high temperatures and pressures but also mechanically fractures the target (Figure 6b). The broken/fractured rocks are subjected to a range of complex interactions during impact, and the disturbance is distributed across different parts of the crater system. French [2] had noted breccia at and below the crater floor, within the crater-fill deposits, and as part of both proximal and distal ejecta deposits. The breccia below the crater floor, produced under lower pressure conditions ($>$2 GPa), is relatively less shocked and mainly consists of broken rock-mineral fragments [36]. The crater-fill deposits contain all the breccia types listed above. The breccia forming the proximal ejecta (thicker deposits) is more susceptible to weathering; meanwhile, the breccia constituting the distal ejecta (thinner deposits) could be modified during atmospheric transport and re-entry [2, 7]. In addition, breccia dikes (cross-cutting the deposits) below the crater floor are also noted, wherein the breccia dikes itself housed a wide variety of breccia types (lithic breccia—melt free; melt-fragment breccia or suevites—melt/glass fragments mixed; melt-matrix breccia—lithic fragments in melt matrix, melt rocks—majorly melt) (cf. [2]). Breccia can be observed at both macroscopic (more prominent) and microscopic scales. Brecciated products form during the contact, compression, and excavation stages of crater formation, although larger units such as breccia lenses or crater-fill deposits form during the modification stage.

8.1.3. Other Ejected Products

The ejection of materials during impact constitutes products such as (micro)dust, condensed particles (from vapourised projectiles), aerosols, and volatiles. During the impact event, the vapourised materials can condense into submillimeter-sized particles, which can thereby remain suspended in the atmosphere for a few weeks to months. For bigger impacts, interactions within the ejecta plume can be more complex. During the Chicxulub event, the conditions and interactions within the dust cloud produced complex products and modified the original products [71] before they were redeposited onto the crust. The identification of such products also remains a crucial aspect to expand our understanding of impact processes. The ejected products form during the excavation stage of crater formation.

8.2. Chemical Products

Chemical products are impactites that can be accurately identified by geochemical and isotopic signatures, since the chemical markers need not be visible in an outcrop or hand specimen. Significant chemical changes of the target are best noted in the melt products (/rocks). Melt products dominantly reflect the action of high temperatures produced by impact cratering. The high temperatures ($>$1500 °C; [7]) melt both the projectile and the target to varying degrees. The levels of melt homogenisation (/mixing) vary with the extent of melting (e.g., bigger projectiles (higher impacting energies) aid more melting). During melt formation (primarily during the excavation stage), the existing geochemistry of the target segments is altered, leading to new melt/glass geochemistry. The melt products can be classified into two, depending on distance from the point of impact, namely (i) proximal and (ii) distal melt products.

Proximal melt products are detected within five crater radii (R) (corresponding to proximal ejecta zones), although the melt volumes will progressively decrease away from the crater center. The proximal melt products can be either macroscopic or microscopic. Megascopic proximal melt products include melt-rich flows, melt-dykes (below crater floor), melt-rich crater-fill impactites, melt lenses, melt veneers [24] (all in and around crater floor), and ejected/brecciated melt rocks/fragments (within 5R distances). These melt products are detrimental in reconstructing the extent of projectile-target interaction (e.g., melt volumes, mixing calculations). Further examination of the megascopic melt product at a much finer scale, through petrographic, spectroscopic, and geochemical analyses, provides a better understanding of the impact

event. The microscopic melt products include lechatelierite (silica glass observed in the melt at $\leq$1750 °C). Furthermore, melt features such as schlieren and ballen quartz (cf. [7]) are more readily observed at the microscopic level. Both features are diagnostic indicators of impact events.

Distal melt products are melt transported to farther distances (>5R) from the impact point. The melt could be exposed to physical (e.g., size reduction, pitting) and/or chemical (e.g., remelting, recrystallization) changes during transport to larger distances. While distal melt products have been found for all craters, studies have shown that larger impacts (e.g., the Chicxulub Impact Event and the Australasian Tektite Event [6]) produced more prominent distal ejecta layers (of semi-global to global extent). Spherules (millimeter-sized; [7]), tektites (natural glass), and some glasses [2] are the most common distal melt products. Distal melt products are more susceptible to weathering and erosion, since these are smaller in size (than proximal melt products), and often manifest as thinner (less continuous) layers, making them less reliable in confirming the impact event.

9. Aftereffects of Impact Cratering

For a kilometer-sized body, the effects of impact can release kinetic energy of about 10^7–10^8 Mt TNT, which will be quickly converted to thermal, seismic, and atmospheric disturbances. Some of the significant impact aftereffects are described below.

9.1. Impact-Induced Seismic Shaking and Mass Wasting

Among the most immediate effects of significant impact events is the intense ground shaking, with estimated magnitudes approaching 10. This is sufficient to transmit elastic waves several crater radii beyond the impact site. It can also trigger extensive slope failure and mass wasting around the impact basin and along continental margins [72]. This extreme shaking destabilizes crater walls and adjacent terrains. This causes large landslides, slumps, and gravitational collapse, significantly modifying crater morphology and redistributing enormous volumes of material. Submarine structures such as the Montagnais and the Chesapeake Bay preserve thick successions of debris flows and slumped units, interpreted as impact-induced margin collapse and gravity-driven reworking of unstable, water-saturated sediments. Moreover, air blasts generated by impacts can reach velocities over 1000 km h^{-1} near the crater. These blasts can create hurricane to extreme-force winds locally reaching $\sim$3500–4800 km h^{-1}, which flatten vegetation, erode soils, and intensify mass-wasting processes over regional scales.

9.2. Tsunami Generation and Marine Impact Effects

Impacts into oceanic or shallow marine environments generate enormous tsunamis, representing one of the most destructive secondary consequences of impact cratering. Numerical modeling and geological observations indicate that marine impacts can generate waves up to 100–300 m high near the impact site. The inundation can extend more than 300 km inland along vulnerable coastlines. The Chicxulub impact caused basin-wide tsunamis, as evidenced by complex deposits found both near and far from the Gulf of Mexico and the Caribbean margin. These include altered spherules, cross-bedded sands, chaotic units, and bioturbated layers preserved in Haiti and the surrounding areas [73]. Shallow-marine impacts such as Montagnais, Mølnir, and Chesapeake Bay produce mega-tsunami waves, resurge currents, and seiche oscillations that erode crater rims. They also generate mass-flow and turbidite deposits both inside and outside the structures. Water-column sloshing during such events prevents classical seafloor cratering while enhancing sediment remobilization and erosion across continental shelves.

9.3. Impact-triggered Wildfires and Ejecta Re-entry Effects

Large impact events produce intense thermal radiation from the impact flash during its atmospheric entry, and from the subsequent re-entry of glowing ejecta. This process is collectively responsible for igniting wildfires on a regional to global scale. For instance, the Chicxulub impact ejecta re-entry triggered extensive biomass burning, producing soot-rich layers that are now preserved in boundary sediments worldwide. The Chicxulub impact also generated a high-velocity ejecta curtain and vapor plume, dispersing melt and target material globally and producing intense, short-lived thermal radiation during the ejecta re-entry. Modeling indicates that ejecta re-entry creates intense heat pulses, strong enough to dry out and ignite vegetation in areas downwind, though widespread fires were probably patchy rather than truly global [72]. Distal tektite and microkrystite horizons associated with large craters such as Ries, Popigai, and Sudbury record high-temperature ejecta transport capable of surface heating enough to trigger regional to continental-scale biomass burning. These observations link large impact craters to ballistic and plume-driven ejecta transport, as well as to impact-induced combustion processes that contributed soot and aerosols to the atmosphere.

9.4. Atmospheric Perturbations and Impact on Winter

Perhaps the most significant effect of large impact events is the major disruption of the atmosphere and climate system. Following the Chicxulub impact, the release of enormous amounts of dust, soot ($\sim10^{17}$ g), and sulfate aerosols into the stratosphere sharply reduced incoming solar radiation. This led to nearly zero surface visibility for several months and initiated an ‘impact winter’ that lasted approximately 6–12 months. Photosynthetic activity was halted for nearly a year. Land-surface temperatures declined by as much as about 30 °C for 1 to 2 years, while ocean temperatures cooled by several degrees. Vaporization of sulfate-rich evaporites released $\sim10^{15}$ mol of H_2SO_4, which increased aerosol cooling. Wildfires added roughly 10^{19} g CO, $\sim10^{18}$ g CH_4, N_2O, PAHs, and photochemical smog, causing a subsequent greenhouse

warming of about 2 to 10 °C over 10^4–10^5 years [74]. These extreme environmental stresses contributed directly to the end-Cretaceous mass extinction, during which more than 75% of species disappeared within roughly 1 to 3.5 million years. Numerical scaling from large Phanerozoic craters like Manicouagan, Popigai, and Morokweng suggests that impacts into volatile-rich sedimentary targets can inject large amounts of dust and sulfate aerosols into the stratosphere. This produces short-lived but severe global cooling events. Stratigraphic studies across these boundaries show negative carbon-isotope excursions and disruptions in productivity, consistent with conditions of a transient impact winter. However, their magnitude and duration appear weaker than those linked to the end-Cretaceous event.

9.5. Oceanic and Biogeochemical Consequences

Marine impacts and large continental impacts that cause significant oceanic fallout can trigger abrupt changes in ocean circulation and nutrient cycling. This includes enhanced upwelling and short-term productivity spikes, followed by longer-term stratification and carbonate undersaturation. For example, impact horizons related to Popigai and Manicouagan coincide with geochemical anomalies and biotic changes. These suggest regional shifts in redox state and export productivity, even in the absence of mass extinction. The collapse of marine primary productivity followed atmospheric darkening. Planktonic foraminifera decreased by about 97%, and calcareous nannoplankton dropped by about 88%. This led to 'Strangelove Ocean' conditions marked by low productivity that lasted for 105 to 106 years. These effects are directly linked to the Chicxulub impact at the K-Pg boundary. Acidification and alkalinity crises halted pelagic $CaCO_3$ production, disrupted the carbon cycle, and caused large fluctuations in pCO_2 and $\delta^{13}C$ values, with recovery spanning ∼130–3000 ka [75].

9.6. Post-Impact Hydrothermal Systems and Long-Term Geological Effects

Large impact structures such as Sudbury, Vredefort, Manicouagan, and Haughton host long-lived hydrothermal systems. These systems are driven by residual heat in impact melt sheets and fractured basement rock. They can last for 10^5–10^6 years. These systems produce extensive hydrothermal alteration halos, metasomatic mineralization, and focused fluid flow along crater faults. This process fundamentally modifies crustal permeability and geochemical reservoirs over geological timescales. Additionally, these long-lived systems also promote localized ore formation and may provide favorable habitats for microbial communities [76]. As a result, impact-generated hydrothermal systems are increasingly recognized as important links between impact cratering, economic geology, and astrobiology [5].

9.7. Biospheric and Deep-Time Implications

Throughout Earth's history, impact events have repeatedly reshaped climatic systems and the biosphere, spanning from the Hadean, which began over 4 billion years ago, through the Archean, Proterozoic, and Phanerozoic eons. During the Late Heavy Bombardment (∼3.9 Ga), large impacts likely caused periods of surface environmental sterilization. At the same time, these events generated long-lived subsurface hydrothermal systems. These sheltered settings may have served as safe environments for early thermophilic life and played a role in the evolutionary origins of modern Archaea and Bacteria. In the Archean rock record, spherule layers from large impact events, such as the S2 impact (∼3.26 Ga), are associated with tsunami-reworked deposits and carbon-isotope signatures that suggest rapid post-impact blooms of microbial communities in iron-rich, nutrient-rich waters. Large-scale impacts later in Earth's history, including the Wilkes Land (∼320 Ma) and Yarrabubba (2229 ± 5 Ma) events, further show how the impacts can disrupt the global climate. These disruptions are especially notable through the vaporization of large ice masses and the possible termination of Paleoproterozoic glaciation.

10. Degradation of Impact Craters

10.1. Terrestrial Craters

Impact craters are subjected to weathering and erosion by agents such as wind, water, glaciers, and mass wasting. Of all these, fluvial erosion plays a prominent role in modifying impact craters, particularly on planets that have had or still retain liquid water. In such cases, crater depressions may become filled with lake deposits and/or alluvium. Additionally, drainage networks in and around impact craters progressively modify their morphology through rim incision, gully erosion, and valley formation [77]. These will later evolve into inlet or outlet formations. Kumar et al. [78] demonstrated that gully erosion, aided by structural weaknesses such as faults, contributes significantly to crater wall degradation, as observed in Barringer. The development of drainage networks depends on water flow strength (discharge rate and velocity), channel morphology, and sediment load, all of which also influence crater modification. These drainage systems typically evolve into radial, centripetal, and concentric patterns [79]. Over time, fluvial activity and other erosional processes gradually erase the surface expression of the craters. On Earth, apart from geological agents, plate tectonics and anthropogenic forces significantly obscure the original crater morphology. Tectonic processes such as crustal recycling, faulting, and folding modify terrestrial craters. Ultimately, time remains the most critical parameter, as the cumulative effects of erosional and tectonic processes determine the extent of long-term crater modification/degradation.

Bolide impacts into marine environments result in marine and submarine craters [73]. Almost all of the marine craters discovered to date have their origins in epicontinental seas [4, 73]. This could be attributed to the increased presence of epicontinental seas in the past, as well as to rapid sediment burial, allowing better preservation than that of deep-ocean impacts like the Eltanin crater [73]. Marine crater degradation can be categorized into five sections, namely physical degradation, sedimentary infilling and burial, tectonic modification, hydrothermal processes, and biological processes. Physical degradation processes include wave and tidal action, marine currents, mass wasting, and collapse features due to submarine landslides. In marine targets, a rim-wave tsunami forms due to the outward collapse of the water cavity and the inward resurge of water from the lower layers, further physically degrading the crater structure. Resurge flow triggers sedimentary infilling and burial of the impact structure. Similarly, the modification stage in the marine impacts results in massive sediment infilling, as witnessed in Chicxulub [80], Mølnir [81], Montagnais [82], Kaluga [83], and Lockne [84]. Tectonic processes such as rift basin activity, faulting, basin subsidence, and salt tectonics modify craters. Subduction is an obvious explanation for the absence of marine craters older than 200 Ma; the oldest confirmed crater is the Mølnir crater at 142 Ma. Basin subsidence and fault-related sedimentation bury both the interior and exterior features of the crater, as seen at Chicxulub. Post-impact hydrothermal processes have been well documented in impact structures [3]. Hydrothermal fluid activity and the subsequently formed mineral assemblages cross-cut shock deformation features and overprint/alter impact lithologies, thus degrading the original impact system. Chicxulub has seen pervasive hydrothermal alteration, especially varied secondary alteration within lithologies in the peak ring region. Biological processes play a lesser but important role in the degradation of marine craters. Studies of impactoclastic layers coeval with both the Chesapeake Bay and Popigai craters show the stratigraphic distribution of Ir due to bioturbation, attributed to *Planolites* and *Zoophycos* burrows. Such stratigraphic redistribution is also witnessed in the Chicxulub crater. The presence of carbonate reef environments in Lockne and Tvären craters, Sweden, masks the original impact textures.

10.2. Martian and Lunar Craters

Fluvial degradation of craters has been documented on Mars [77] and Titan [85]. Martian craters have witnessed fluvial activity during early times. The most important evidence of fluvial activity on Martian impact craters is valley/crater rim incision, the presence of alluvial fans and deltas, and the resulting erosion or burial of impact craters [86]. On the Moon, due to the absence of an atmosphere and minimal internal geological activity, most small craters degrade differently. Fresh, small craters become shallower over time until they are no longer visible. This process, called diffusive degradation, is caused by the cumulative effects of craters forming in the surrounding area. Smaller craters are only rarely removed by the direct overlap of larger craters, known as 'cookie cutting'. Alternatively, large craters are more likely to be lost by cookie cutting [87].

11. Significance of Studying Impact Craters

11.1. Primitive Composition of the Solar System

Younger impact craters are suitable locations for direct sampling of extraterrestrial materials that reflect the primitive composition of the solar system. This forms one of the major reasons for studying impact craters. The precise identification of impactors helps document the origin and frequency of different types of projectiles that have impacted Earth's surface. The Oort Cloud and the Kuiper Belt are believed to be the main sources of comets. But for the Earth-Moon system, the percentage of cometary impactors is very low (∼1%) [88]. Comets are reported to have a small proportion of non-volatile elements, which makes their identification difficult. The asteroid belt, located between the orbits of Mars and Jupiter, is the main source of asteroids. Meteorites are fragments of these asteroids, sometimes fragments derived from the Moon and Mars as well. So, in addition to direct sampling, asteroids can be studied through the remnants found in and around impact craters. Asteroids are unaccreted small fragments remaining from the original protoplanetary disk after planet formation. They get suspended in the terrestrial planet-forming region and wander the solar system in unpredictable paths influenced by the gravity of larger planets. Asteroids, having formed during the early stages of the solar system, preserve primordial material and thus act as tracers of planetary formation and evolution. Asteroids are divided into two groups: undifferentiated and differentiated asteroids. Undifferentiated asteroids, which have undergone some metamorphism without melting, are the parent bodies of chondritic meteorites. These asteroids appear not to have undergone major element fractionation after their formation. Therefore, based on the composition of the single meteorite, it is possible to retrace the composition of the entire parent body. Some meteorites, despite showing notable degrees of shock and volatile-element depletion, maintain constant ratios of refractory and moderately volatile elements, serving as fingerprints for different chondrites. On Earth, 85% of the observed meteorite falls are identified as chondrites, making undifferentiated meteorites/asteroidal materials the most common extraterrestrial material reaching Earth. Differentiated asteroids that have undergone melting and partial or complete metamorphism are the parent bodies of achondrites, stony-iron meteorites, and iron meteorites. Thus, the traces of meteoritic material identified in meteorite impact craters provide insights into the primitive composition of the solar system.

11.2. Origin of the Moon

The Moon is the only natural satellite of Earth and helps stabilize Earth's axial tilt, making Earth a suitable location for life. In the early stages of planetary science

studies, the Moon's origin was one of the most debated topics [89]. The Giant Impact Hypothesis (GIH) is the most widely accepted theory, offering a solution to the dynamical, geochemical, and physical constraints on the Moon's origin that other models cannot explain. GIH states that a Mars-sized planet (theorized to be called Theia) collided with the proto-Earth roughly 4.5 billion years ago. The collision would have resulted in debris and vapor being expelled from the Earth into space. Over time, that debris was brought back together through strong gravitational forces to form the present-day Moon. First, this hypothesis accounts for the Moon's low density and small iron core, since most of the iron from the impactor and Earth would end up in Earth's core, while the Moon accreted largely from silicate-rich mantle material. Second, the depletion of volatile elements in the lunar samples is readily explained by extremely high temperatures inferred during the impact, which led to the loss of volatiles from the debris disk. Third, the angular momentum of the Earth-Moon system cannot be reproduced by capture-and-fission models without invoking unrealistic conditions, a fundamental problem GIH does not face. Finally, numerical simulations demonstrate that high-energy impacts can generate extensive mixing between Earth and impactor, thus providing the first clear explanation for the remarkable isotopic similarities between Earth and Moon for O, Ti, Si, W, and possibly Hf–W. When all these factors are taken together, GIH remains the most plausible and complete model for explaining the Moon's origin.

11.3. Space Weathering and Regolith Formation in Airless Planetary Bodies

Space weathering encompasses the physical, chemical, and mineralogical alterations that affect the surfaces of airless planetary bodies due to prolonged exposure to the space environment [90]. The concept of space weathering was first recognized through analyses of returned lunar samples, which revealed physical and spectral modifications in lunar soils relative to their parent rocks. Subsequent integration with remote sensing observations of the Moon enabled a more comprehensive understanding of surface alteration processes, a framework that has since been extended to Mercury and other airless planetary bodies [91].

The fundamental drivers of space weathering on airless planetary bodies are micrometeoroid impacts, solar wind implantation, and cosmic irradiation. Unlike Earth, where most micrometeoroids are ablated in the atmosphere, airless bodies are directly exposed to continuous micrometeoroid impacts. Particles ranging in size from microns to several millimeters strike these surfaces at hypervelocity with impact speeds of ∼4–5 to 70 km s^{-1} (average: ∼20 km s^{-1}), producing craters with characteristic diameters from approximately 1 μm to 1 cm [92]. Even at relatively modest velocities of ∼5 km s^{-1}, these collisions are energetic enough to induce molecular fragmentation and chemical alteration of both the impactor and the target materials (Figure 12).

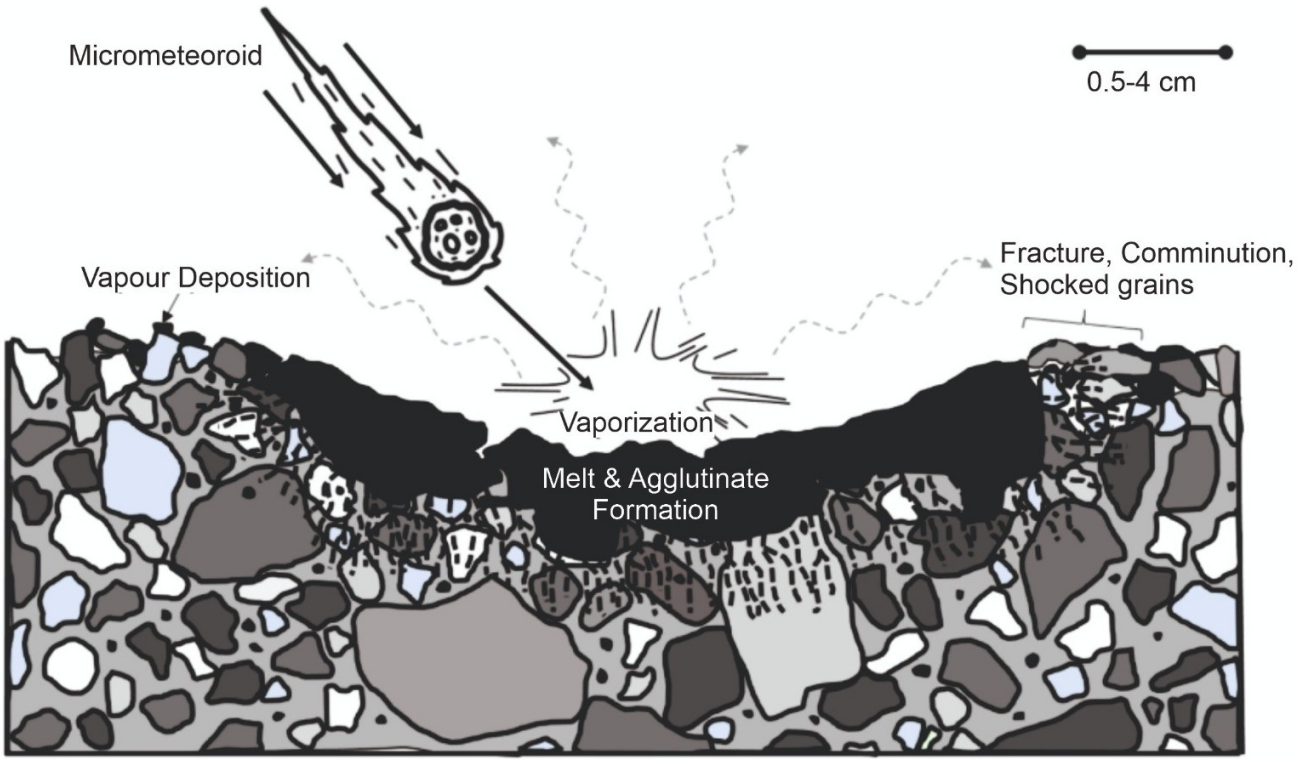

Figure 12. Schematic illustration of micrometeoroid bombardment as a component of space weathering on airless bodies. The diagram summarizes the constituent processes associated with micrometeoroid impacts and their effects on the near-surface regolith (*Modified after* Pieters & Noble [17]).

Micrometeoroid bombardment alters regolith primarily through two coupled mechanisms: impact gardening and impact-induced melting and vaporization [90]. Impact gardening involves repeated excavation, fragmentation, burial, and lateral mixing of surface materials, progressively breaking down bedrock and clasts into fine-grained regolith while homogenizing the upper layers. On the Moon, the upper $\sim$2 cm of regolith is reworked over $\sim 10^5$ years, with more efficient reworking expected on Mercury due to higher impact velocities and fluxes.

The second mechanism is when micrometeoroid impacts generate localized melting and vaporization of both target and impactor material. Rapid quenching produces agglutinates, while vaporization preferentially removes volatiles and recondenses fewer volatile elements, particularly iron, forming nanophase metallic iron (npFe$^\circ$) coatings on nearby grain surfaces. The accumulation of npFe$^\circ$ is the defining mineralogical consequence of micrometeoroid-driven space weathering and dominates surface optical properties. Increasing npFe$^\circ$ abundance causes progressive darkening, attenuation of diagnostic mineral absorption bands, and reddening of spectral slopes [93]. These trends are observed in lunar soils, Mercury [94], and asteroids such as Ryugu [95] and Bennu [96], indicating that micrometeoroid impacts are a primary mechanism governing optical maturation on airless surfaces.

11.4. Crater Size-Frequency Dating of Planetary Surfaces

Impact cratering can be analyzed at the scale of single features or as a statistical population. As a result, the number and distribution of preserved impact craters on a given terrain provide a quantitative measure of its relative age. Relative surface ages of an area are inferred from crater density and superposition relationships and are particularly significant for deciphering the surface ages of airless planetary bodies that experience minimal surface modification. To quantify these crater populations, crater statistics are commonly expressed using crater size–frequency distributions (CSFDs), which describe the abundance of craters as a function of diameter and form the basis of crater-based surface dating. The calibration of this method can be done by linking the radiometric ages of surface samples to the corresponding remotely derived CSFD of the surface. The Moon is the only planetary body for which samples have been collected from multiple locations by the Apollo, Luna, and Chang'e missions, enabling calibration of the lunar crater chronology. These calibrations form the basis of crater retention–age models for the Moon [97, 98], which are subsequently scaled and applied to other inner Solar System bodies including Mars [97], Mercury [99], Venus [100], Vesta [101], and Ceres [102] after accounting for interplanetary variations in impact flux, gravitational focusing, impact velocity, and target material properties [1].

The mathematical framework underlying CSFD analysis is built upon two interrelated components: the Production Function (PF) and the Chronology Function (CF). The PF describes the relative abundance of craters as a function of diameter produced by a given impactor population, reflecting the strongly size-dependent nature of impact rates in which small impactors are far more frequent than large ones. The CF relates the cumulative number of craters commonly referenced to diameters $\geq$1 km to absolute time, thereby enabling quantitative surface age determination [98].

In practice, crater-based age determination begins with systematic crater counting, which involves identifying and mapping impact craters superposed on a well-defined surface unit. This process requires accurate delineation of the counting area, careful crater identification and classification, precise measurement of crater diameters, and complete sampling of the crater population above a selected minimum size. Surface ages are then obtained by fitting the observed CSFD to an established PF and applying a calibrated CF to crater frequencies over selected diameter ranges. CSFDs are typically visualized as log–log plots using cumulative (Figure 13), differential, or relative (R) representations, which differ in their crater density metrics and binning strategies. Deviations from the expected production function, often referred to as kinks, are particularly significant, as they commonly indicate resurfacing or modification events [103].

The precision of CSFD-derived ages, however, is inherently limited by geological and statistical sources of uncertainty. Secondary cratering, produced by the re-impact of ejecta from primary events, can artificially inflate crater counts and lead to overestimated ages if not rigorously filtered. In addition, ancient surfaces may approach crater equilibrium, where the formation of new craters is balanced by the degradation of existing ones, effectively saturating the chronometer [104]. Despite these limitations, integrating CSFD analysis with high-resolution orbital imagery remains the most robust method for reconstructing the long-term impact and resurfacing history of solid bodies in the Solar System.

11.5. Orogenic Processes Associated with Impact Cratering

Orogenic-style processes related to large impact cratering can be understood through Rheasilvia, a $\sim$500 km-diameter impact basin on Vesta (Figure 14). It serves as a clear example of how a single massive impact can lead to crustal flow, structural uplift, and long-lived modification that resemble orogeny, even though they result from an external impact rather than plate convergence. In hypervelocity impacts, the modification stage is responsible for 'orogenic-like' rock flow, uplift, and large-scale faulting [105]. Similar processes are also observed in Chicxulub, where drilling and geophysical data reveal that peak rings are composed of deeply uplifted, shocked, and highly fractured basement rocks (with increased porosity and reduced density) [106]. These rocks are transported upward along large shear zones due to quasi-continuous rock flow, leading to renewed strength and ring formation [106]. These rapid, large-scale rock flows and crustal reconfigurations are analogous to crustal thickening and exhumation in orogens, but occur in minutes rather than millions of years [106].

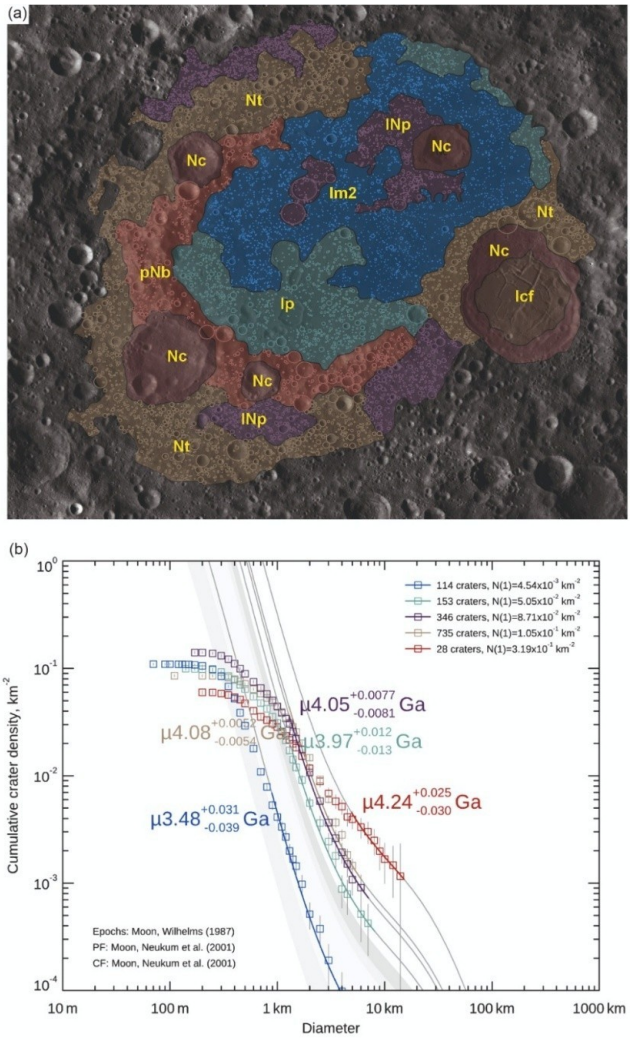

Figure 13. Geological context and crater size–frequency dating (CSFD) of Mare Moscoviense on the Moon (**a**) Geological units of Mare Moscoviense (after Fortezzo et al. [107]), overlain on the Lunar Reconnaissance Orbiter Wide Angle Camera (LROC WAC) basemap. Units include pre-Nectarian basin (pNb), Nectarian terra (Nt), Nectarian crater (Nc), Imbrian–Nectarian plains (INp), Imbrian plains (Ip), Imbrian upper mare unit (Im2), and Imbrian crater-fractured floor (Icf). Crater populations mapped for age determination are shown within their respective units. The scale bar denotes 100 km. (**b**) CSFDs for selected units, with crater populations color-coded by geological unit. Best-fit Neukum production and chronology functions are shown, along with derived absolute model ages (AMAs) and associated 1σ uncertainties.

Large impact basins, therefore, generate circular crustal domains that are intensely fractured and thermally altered, and that have evolved through both rapid dynamic collapse and much longer-lived post-impact adjustment. The initial collapse produced peak rings, scarps, and floor lineations, whereas subsequent isostatic readjustment and tectonic modification led to floor fracturing, uplift, and peripheral subsidence over extended periods. On Earth, Sudbury and Vredefort impact basins show how these mechanically weakened regions can later be affected by regional orogeny. Long-term crustal relaxation combined with external shortening results in folding, shear zones, and metamorphism that reorganize basin architecture and remobilize minerals. This phenomenon highlights a two-stage coupling between impact processes and orogenic deformation.

Hydrocode simulations of multiring basins, including Orientale on the Moon, show that the flow of warm, mechanically weak material at depth during crater collapse is crucial for the development of outer rings. These rings are often seen as large normal-fault systems. In the models, the spacing and position of the rings depend heavily on the impactor's size and the lithosphere's thermal structure. Remote-sensing, experimental, and numerical studies suggest that Rheasilvia and similar impact basins act as rapid, impact-driven analogues to orogens. Transient processes such as acoustic fluidization and large-scale rock flow lead to crustal thickening, uplift, and ring-belt faulting. Meanwhile, longer-term relaxation, secondary tectonism, and externally imposed stresses exploit the impact-weakened lithosphere to generate rings, troughs, scarps, and shear zones. These features resemble collisional belts, despite reflecting a fundamentally different, highly impulsive geodynamic mechanism [106].

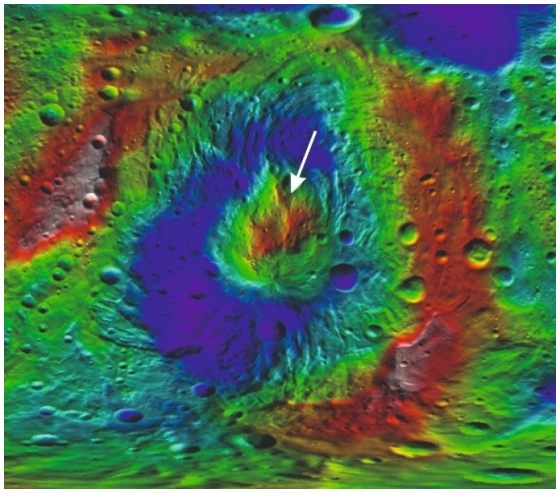

Figure 14. Colorized topography of the Rheasilvia impact basin on asteroid Vesta, showing relative elevation variations derived from the Dawn Framing Camera Digital Terrain Model (DTM). Warm colors denote higher elevations, while cool colors represent lower elevations. The basin exhibits extreme relief between the central uplift and the surrounding basin floor and rim. Data accessed and visualized using JMARS (Figure not to scale).

11.6. Initiation of Plate Tectonics

The probable mechanisms discussed in the scientific literature on impacts and their influence on tectonic processes include thermal weakening, crustal fracturing and fault network formation, initiation of subduction, impact-driven mantle convection and plume initiation, stress reorganization and horizontal tectonic forces, and coupling of impact processes with crustal recycling and magmatism.

Thermal reference models highlight how thermally altered regions and thick melt sheets form due to large impacts, weakening lithospheric strength and making it susceptible to gravitational collapse, delamination, and localized downwelling [108]. Another hypothesis considers the impact as the cause of the formation of early cratonic regions, due to impact-induced partial melting of mantle material, which then solidifies into the crustal portion of a craton. Meteorite impacts have also been hypothesized to have initiated subduction, especially in the early Earth lithosphere, which was thinner and hotter. Subduction, triggered by large impacts, could have occurred intermittently as part of episodic tectonics, helping to localize crustal recycling. The hypothesis of an impact-induced origin of plate tectonics is not limited to Earth alone. Large oblique impacts on Mars have been postulated to have caused a mantle thermal anomaly that drove decompression melting and sustained magmatism, forming the volcanic province of Tharsis. Thus, meteorite impacts might not have been the primary driver of plate tectonics; however, they played a crucial role in Archean tectonics by locally weakening the lithosphere, triggering episodic subduction-like events, and crustal recycling [108].

11.7. Formation of the Rings of Saturn

The origin and age of Saturn's main rings remain long-standing questions in planetary science. One of the earliest and most influential hypotheses proposes that the rings were formed from the destruction of a mid-sized, Mimas-scale satellite (radius $\sim$200 km) following a collision with a heliocentric impactor. This hypothesis was framed owing to the similarity between the total mass of the rings and that of a typical Saturnian mid-sized moon.

According to this theory, a Mimas-mass moon orbiting approximately 105,000 km from Saturn could be destroyed, generating the small icy particles that now make up the rings, during a period of enhanced impact flux comparable to the LHB. Assuming an impact velocity of $\sim$34 km s^{-1}, the disruption of an icy satellite with a radius of $\sim$200 km would require an icy impactor with a radius between 10 and 20 km.

One challenge for this hypothesis is the nearly pure ice composition of Saturn's rings. A disrupted satellite would normally produce debris containing silicates, yet the rings are dominated by ice [109]. If the progenitor moon was differentiated, with a dense silicate core surrounded by an icy mantle, the impact could preferentially remove the icy outer layers while leaving the core largely intact. This mechanism is consistent with numerical simulations of large-scale impacts associated with the formation of the Moon and the Pluto–Charon system, in which the target's core remains largely intact while the mantle material is preferentially ejected [110].

Estimates of the rings' age are uncertain. Models suggest they could have formed either during Saturn's early history or during the Late Heavy Bombardment, implying ages of approximately 3.8–3.9 to 4.5–4.6 Gyr. However, measurements of space-weathering effects on ring particles indicate much younger ages, ranging from 10^5–10^9 years [111], with the estimates being later refined to $\sim$4–400 Myr based on Cassini-era measurements. This discrepancy highlights a continuing tension between dynamical formation models and observational constraints.

Despite these unresolved issues, the collisional disruption hypothesis remains one of the leading explanations for the origin of Saturn's rings, alongside alternative scenarios involving tidal disruption of comets or remnants of Saturn's primordial disk.

11.8. Opposite Revolution of Venus

Venus most closely resembles Earth. However, it has surface conditions that are drastically different from Earth, including surface pressures exceeding 90 times Earth's atmospheric pressure, mean surface temperatures of about 740 K, a carbon-dioxide–dominated atmosphere, and clouds composed of sulfuric acid [112]. Venus exhibits a slow retrograde rotation, which separates it from all other terrestrial planets and has been the subject of extensive investigation. There are several theories explaining Venus's retrograde rotation. Early studies showed that thermal atmospheric tides, driven by solar heating, can exert significant torques capable of modifying Venus's rotation rate and direction. Later, Coleman et al. [113] explored the idea of an asteroid colliding with a young Venus with a rotational period similar to Earth's, imparting enough kinetic energy to reverse its rotation. Their results showed that an asteroid moving at 35 km with a mass of 3.1×10^{20} kg would produce enough kinetic energy to overcome Venus's rotational kinetic energy, and reverse the planet's rotation. The latest study by Bussmann et al. [112] examines the feasibility of a late giant impact on Venus by a Mars-sized differentiated body, using numerical impact simulations spanning a range of impact angles, velocities, and pre-impact spin states. The study demonstrated that such an impact can efficiently modify Venus's angular momentum, producing a slow or retrograde rotation consistent with present-day observations without requiring extreme initial conditions. The simulations further show that most impact scenarios generate only small debris disks that rapidly reaccrete, providing a plausible explanation for the absence of a Venusian moon. Overall, the results support an impact as a viable mechanism influencing Venus's rotational evolution and early physical state, analogous in scale but distinct in outcome from Earth's Moon-forming event.

11.9. Origin of Life and Sterilization of the Planet

Meteorites act as agents delivering organic molecules from space. Thus, impact craters may have played a significant role in the origin of life, as they facilitated the exogenic delivery of key ingredients during the cosmogenic stage [5]. Additionally, craters provided a chemical environment for the formation and evolution of cellular components. Impact craters sometimes develop hydrothermal systems, providing both ingredients and environment for the origin of life. The Earth's earliest ecology may have provided the environment for the first spark of life, which may have taken the form of RNA or single-cell organisms. In recent years, advances in space exploration have shifted the study of the origin of life to a broader perspective, encompassing planetary origins and exobiology. Some of the building blocks of life have been detected in Murchison meteorites, such as nucleotides of DNA and RNA, 70 extraterrestrial amino acids, cell membranes, hydrocarbons, and carbonyl compounds. As they are 4.6 Ga old, asteroids provide evidence that life's building blocks originated from icy interplanetary dust and were then carried to Earth. Additionally, comets contain prodigious quantities of organic compounds, including amino acids, adenine, ketones, quinones, carboxylic acids, hydrogen cyanide, polycyclic aromatic hydrocarbons, thioformaldehyde, acetaldehyde, sugars, cyanogens, cyanide, methanol, and ethanol. Smaller comets or cometary dust probably delivered prebiotic molecules that were freeze-dried and preassembled to early Earth, but the hydrothermal crater basin was the crucible of life.

The hydrothermal crater-lake environment had a chemical composition that enabled the symbiotic assembly of the first cells, which were capable of reproduction, heredity, variation, and natural selection. There are several theories for the origin of life: (i) a hierarchical model of the origin of life; (ii) hydrothermal impact crater-lakes as a favourable environment for the emergence of life; (iii) the RNA world may have been the RNA/protein/lipid world; and (iv) serial endosymbiosis of encapsulated RNA and protein molecules led to the origin of the first cells. The earliest history of Earth during the Hadean period is poorly recorded in the geologic record but is reconstructed from the impact history of the Moon and the inner planets. When the Earth formed some 4.6 Ga, the planet was sterile and inhospitable to life, with erupting volcanoes, falling meteors, and a hot, noxious atmosphere of steam. The Hadean Earth was a fiery globe of molten crust generated by relatively heavy bombardment of meteorite impacts; the atmosphere was thick and opaque to thermal radiation, and the climate was dominated by internal heat. As the frequency of impacts slowed at the beginning of the Archean, Earth cooled, clouds formed, and the crust began to harden, creating terrain. Understanding the environment in which the continental-type crustal rocks of Earth formed provides an important perspective and timeframe for the conditions on early Earth that enabled the synthesis of life.

Deep-sea hydrothermal vents, characterized by high temperature and high pressure, have been considered as possible cradles of early life. These sites are geochemically reactive habitats, where microbial life thrives today around superheated water supporting diverse chemosynthetic ecosystems. One crucial precondition for the origin of life is that comparatively simple biomolecules must have had the opportunity to form more complex molecules by segregation and concentration. So perhaps sequestered crater lakes with hydrothermal systems were the best environments favoring organic reactions on early Earth. Life must have originated in an environment isolated from UV radiation and the global oceans to facilitate the concentration of prebiotic soup. Complex organic molecules are vulnerable to damage from sodium and chlorine in seawater, making crater lakes a suitable location.

This hydrothermal crater lake, reconstructed from the early-Earth environment, is the terrestrial equivalent of the habitable environment of Gale Crater on Mars, characterized by neutral pH, low salinity, and variable redox states of both iron and sulfur compounds. Impact craters are of great interest in planetary exploration because they are considered potential sites for evidence of life. The high K^+/Na^+ ratio and relatively high concentrations of Zn, Mn, and phosphorus compounds of living cells support the geothermal terrestrial origin of life. This finding challenges the widespread view that life originated in the sea, but favors the freshwater impact crater basin as the likely crucible. Hydrothermal systems in crater lakes are particularly regarded as sites where primitive life could evolve.

The origin-of-life debate has centered on whether genes or metabolism arose first. The defining characteristics of life include metabolism, storage, and duplication of genetic information. Protein is an essential component of metabolism, whereas nucleic acid is a prerequisite for replication. The most striking feature about cellular life is the ubiquity and universality of this dual structure, replication, and metabolism. Among several competing hypotheses for the origin of life on Earth, the 'RNA world' model is widely accepted despite the complexity of RNA synthesis. Naturally occurring RNA molecules possess very few of the specific enzymatic properties of proteins. Proteins make all RNAs, and there is no evidence from evolution that RNA was ever produced by RNA itself. The building blocks of life may have originated in the tiny icy grains that make up the gas and dust in interstellar space, and those grains could be the key to understanding how life arose on Earth. These organic molecules were formed as a by-product of the explosion of a nearby star during the beginning of our Solar System (>4.6 Ga) [114]. Finding these biomolecules in an interstellar gas cloud means that important building blocks of life, such as membrane-forming molecules, amino acids, nucleobases, sugars, and many organic compounds, were seeded on the primordial Earth through meteorites and interstellar dust. Recently, the Rosetta Mission of the European Space Agency (ESA) craft, Philae Lander, has already detected water and organic molecules on the surface of 67P/Churyumov-Gerasimenko. These 4 km-wide comets may shed new light on the composition of the building blocks.

11.10. Origin of the Hydrosphere

The origin of the hydrosphere and the further evolution of life are expected on rocky planetary bodies that possess liquid water under suitable physicochemical conditions [115]. Comets are primitive icy bodies composed of water ice, frozen gases (CO_2, CO, NH_3, CH_4), and a wide range of organic compounds, dust, and rock fragments. Based on geochronological evidence and dynamic models, Gomes et al. [20] suggest that intense bombardment of rocky planets during the LHB (∼4.1 to 3.8 Ga) would have delivered comets and planetesimals into the terrestrial region. During comet impacts on terrestrial planets, substantial amounts of water and other volatiles could be released, potentially augmenting surface and atmospheric reservoirs. Marty [116] suggests that the contribution of comets to terrestrial water, carbon, and nitrogen may be less than 1%.

Cometary water exhibits a wide range of hydrogen-isotopic compositions, indicating chemical diversity among comet populations, such as the Oort Cloud Comets (OCC), in odds with a potentially single, uniform source [117]. Early studies indicate comets with D/H ratios 2–3 times higher than Earth's oceans [118] in several OCCs. But the Jupiter family comets (JFCs) carry a limited range of D/H ratios similar to that of terrestrial ocean water. Some JFCs have measured D/H ratios similar to terrestrial ocean water, such as Comet 45P/Honda-Mrkos-Pajdušáková, Comet 46P/Wirtanen ($\sim 1.6 \times 10^{-4}$), and Comet 103P/Hartley 2 [119].

Viscous spreading (post the protoplanetary disc formation) along with late-stage molecular cloud infall might have resulted in redistribution and late-stage differentiation of high D/H water to the inner disc region and low D/H water to the outer disc region [119]. By scaling out the effects of secondary processes, the original isotope ratios of water on Earth, Mars, and Vesta, as well as those of C- and S-type asteroids, indicate a refined range for δD of 100‰ to −590‰. Hallis [117] inferred that these terrestrial planetary bodies might have sourced water from the bombardment of C- and S-type asteroids. Cordiner et al. [120], in their study using Atacama Large Millimeter/submillimeter Array (ALMA) and NASA's Infrared Telescope Facility (IRTF), reported that Halley-type comet 12P/Pons-Brooks, with intermediate orbital periods (between 20 and 200 years), has a D/H ratio of $(1.71 \pm 0.44) \times 10^{-4}$; statistically indistinguishable from terrestrial seawater. This is the lowest measured ratio among the different cometary classes and is at the lower end of the cometary values observed so far. Tracing the isotopic composition of water provides a powerful tool for reconstructing the transfer of water from interstellar reservoirs into the protoplanetary and planetary systems. Isotopic evidence indicates that comets have a broad range of D/H ratios in water, reflecting diverse formation environments in the early Solar System. Several comets, especially from JFC, show D/H composition similar to Earth's oceans, strengthening the idea that at least some comets could have contributed water to early Earth and complemented the planet with volatile inventories and organics.

11.11. Mass Extinction

Bond and Grasby [121] list 17 mass extinction events since the Early Cambrian. Of these, the 'Big Five Mass Extinctions' are the End-Ordovician Major Biodiversity Crisis (444 Ma), the Late Devonian Major Ecological Crisis (371.9 Ma), the End-Permian Mass Extinction (251.9 Ma), the End-Triassic Major Ecological Crisis (201.3 Ma), and the End-Cretaceous Mass Extinction (66 Ma) [122]. The trigger for the End-Cretaceous Mass Extinction (66 Ma) was established as an asteroid strike at Chicxulub (Mexico) [6, 71], with likely contributions from Deccan Volcan-

ism as well. But the remaining mass extinctions are not as well linked to impact cratering events as the Chicxulub impact. Hence, the focus of future studies should be on more strongly linking impact signatures to mass extinction events, while attempting to understand the various ways in which impacts can ultimately lead to a mass extinction.

11.11.1. Chicxulub Impact Event—The Only Impact Conclusively Tied to a Mass Extinction

The Chicxulub crater was forged onto the Yucatan Peninsula at 66.052 $\pm$ 0.043 Ma [11] by a carbonaceous chondritic impactor, impacting at an inclined angle of 45–60° (to the horizontal). The asteroid of 10–14 km diameter, on hitting the target at an impact velocity of 12–15 km s^{-1}, generated impact energies of 2.2 $\times$ 10^{22}–7.4 $\times$ 10^{22} J [19]. The energy estimates pertain to the vertical impact model of Ivanov [19]; though energy calculations for an oblique impact (20–30°) scenario would differ, as depicted by Rampino [87], yielding an energy equivalent of 6.3 $\times$ 10^{23} J. The target was rich in Ca-carbonate and Ca-sulfate [14]. Stratigraphic examinations of the Yucatan Peninsula reveal that the impact site had an approximately 3 km-thick sequence consisting of dolomite, limestone, anhydrite, sandstone, and shale.

The outcome of the impact can be assessed on two spatial scales: (i) regional and (ii) global. The regional scale evaluates the ramifications of the impact across the immediate surroundings (within proximal ejecta distances of 1000 km). This value is in close proximity to the radius of blast damage (of ~6 crater diameters) of 1000 km provided by Rampino [87]. The 45–60° impact ejects proximal and distal ejecta symmetrically from the crater center. As a result, the proximal region contains the maximum density of impact ejecta. The enormous amounts of ejecta ultimately buried the region [14]. The impact triggered tsunamis that radiated into the Gulf of Mexico, the proto-Caribbean, and the Atlantic basins [14], while the region experienced earthquakes of magnitude greater than 10 [87]. The region has experienced the global effects of impact events on a much more devastating scale.

A slew of global events followed the impact, though the timing and effectiveness of some remain speculative. The global changes in temperatures form part of these global changes. Chicxulub's radiational effects had the potential to trigger global wildfires [72, 87], although only significant landmass connectivity can ensure such a scenario. The presence of vast amounts of dust, aerosols, water, and soot in the atmosphere prevented sunlight from reaching the surface, inhibiting plankton photosynthesis [14]. The finer particles (especially submicron material and soot) were retained in the atmosphere for longer time spans [14]. The extent of atmospheric opacity is quantified by Rampino [87] for different amounts of submicron dust, with optical depths over 200 being responsible for a global impact winter (cf. [87]). Owing to the impact, the atmosphere above will be shock-heated to produce NO_x [14], and will additionally witness an incorporation of huge amounts of sulfur (100–500 Gt), derived significantly from the anhydrite target, to generate sulfate aerosols [14, 74]. The above phenomenon results in a combination of nitric acid rain and sulfuric acid rain [14]. The asteroid and target vaporization added large quantities of Cl, Br, CO_2, CH_4, and H_2O to the atmosphere, suggesting potential ozone loss and a greenhouse effect on the planet [14]. Ultimately, the relative prominence and combination of one or more of these global events triggered by the Chicxulub impact led to the K-Pg mass extinction.

The K-Pg Mass Extinction led to the loss of ~76% of all species, and 40–47% of genera loss [122]. Longrich et al. [123] noted that non-avian dinosaurs and pterosaurs became extinct; meanwhile, large reptiles (marine and flying) and Mesozoic invertebrate clades (ammonites, belemnites, rudists, inoceramid bivalves) also disappeared at the species level [122]. Racki [122] noted that foraminiferans, sponges, brachiopods, molluscs, and marine reptiles were more affected by the extinction than other groups. Approximately 50% genus loss in marine communities, whereas lesser losses in freshwater communities due to their better adaptability to changing environmental conditions. The large-scale extinction is a direct result of the breakdown of the food chain from the bottom. The lack of sunlight (hence, photosynthesis) for prolonged periods (e.g., several months to years; Pierazzo et al. [74]) and slower photosynthesis recovery (Milne and McKay [124]) could cause starvation even higher up the food chain, leading to the extinction of larger marine organisms. Kaiho et al. [125] noted that freshwater species (~90%; detrital feeding) survived compared to the land species (~12%; primary productivity). Furthermore, >80% land plants underwent extinction. In the remaining living species that did not undergo major extinction, size and diversity were drastically reduced. Hence, this crisis on both ecological and biodiversity fronts together [122] led to the K-Pg mass extinction.

11.12. Mineral Deposits Associated with Terrestrial Impact Craters

Mineral deposits associated with terrestrial impact craters form through an extraordinary chain of geological processes initiated at the moment a bolide strikes the Earth and continuing throughout the long-term evolution of the crater structure [12]. Unlike endogenous ore-forming systems driven by magmatic, metamorphic, or sedimentary processes operating over millions of years, impact-related mineralization is triggered by a sudden, catastrophic event that generates extreme pressures and temperatures for only fractions of a second [13]. Despite this brevity, impact cratering can initiate a diverse spectrum of mineral systems, ranging from shock-generated phases and impact melt-hosted ores to hydrothermal, sedimentary, and hydrocarbon deposits (formed during prolonged post-impact modification; Osinski et al. [3]).

Following the classification originally proposed by Grieve and Masaitis [12], and further developed by Grieve [13] and subsequent authors, mineral deposits associated with impact structures can be broadly classified as progenetic, syngenetic, or epigenetic [12, 13] (Figure 15). These

categories represent end-member processes rather than discrete stages, and their relative importance depends on crater size, impact energy, target lithology, and the post-impact thermal and hydrological evolution of the structure [3].

11.12.1. Shock Metamorphism and Early-stage Mineralization

The initial stage of mineralization begins with shock metamorphism. Extreme shock pressures induce the instantaneous transformation of minerals into high-pressure polymorphs and the partial or complete melting of target lithologies.

In addition to forming new mineral phases, shock processes mobilize and redistribute metallic elements. In mafic or sulfide-bearing crustal units, the shock wave may volatilize or remobilize metals, producing heterogeneous enrichments that later interact with melt and hydrothermal fluids. Following the compression stage, the release or decompression phase generates intense fracturing, producing breccias and increasing the permeability of target rocks. This structural disruption provides pathways for (later) melt migration and hydrothermal fluid flow, setting the stage for multi-phase mineralization as the crater evolves [3].

Progenetic mineralization: Impact modification of pre-existing ores

Progenetic mineralization refers to ore deposits that were present as surface/subsurface deposits before the impact event but were subsequently modified by shock deformation, uplift, and large-scale structural reorganization [12, 13]. In such cases, the impact does not generate new mineral systems but can significantly alter ore geometry, accessibility, and metal distribution.

The Vredefort Dome in South Africa provides the most prominent example of progenetic mineralization. The gold and uranium deposits of the Witwatersrand Basin predate the impact by more than a billion years, yet the impact event thermally altered ore-bearing strata, reactivated fluid pathways, and contributed to the redistribution of gold within the basin [13]. This example demonstrates how impact events can profoundly modify world-class ore systems without serving as triggers for any apparent mineralization [76].

Syngenetic mineralization: Melt-driven ore formation

Syngenetic mineralization encompasses deposits formed directly by the impact event, either during shock compression or through processes associated with impact-melt generation and cooling [12, 13]. In large impact structures, the volume of melt generated during excavation can reach thousands of cubic kilometres, forming extensive melt sheets that behave similarly to large magma chambers [13]. As these melt bodies cool, they undergo differentiation, assimilation with target lithologies, and segregation from immiscible phases, creating highly effective ore-forming environments [126].

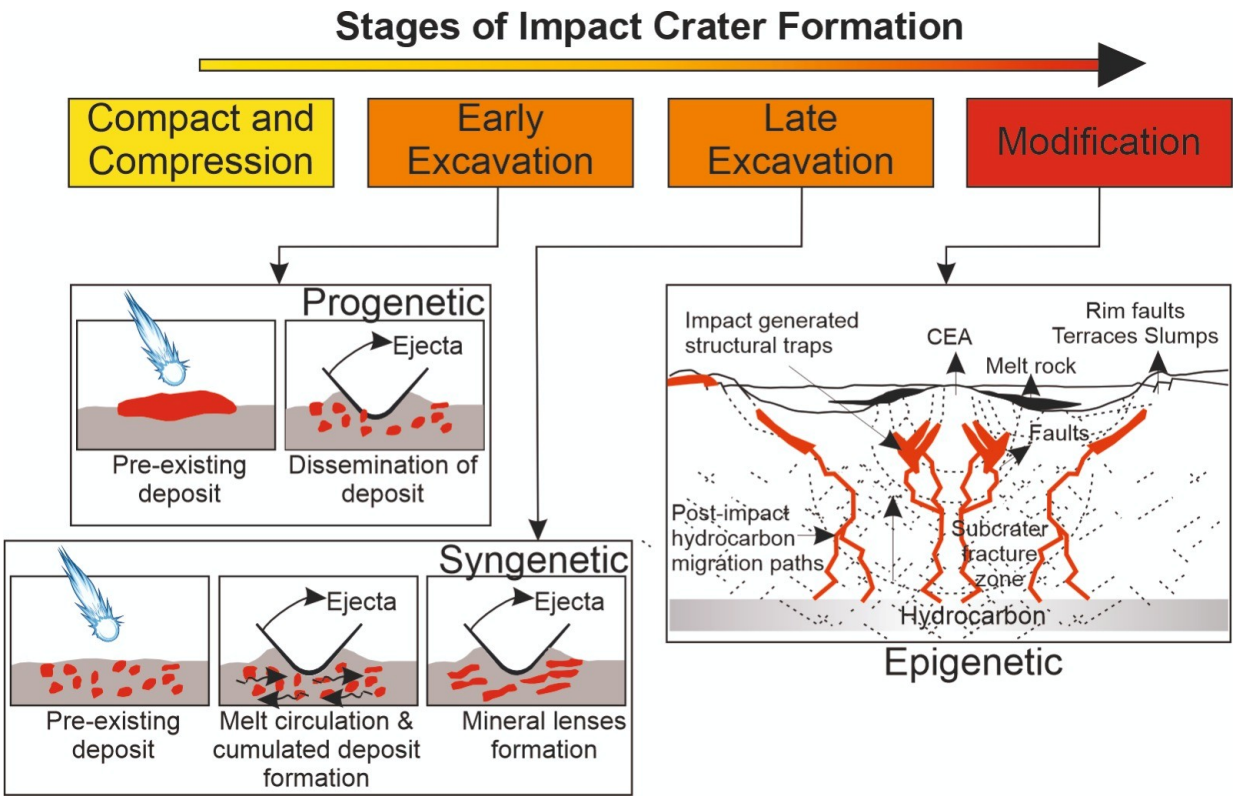

Figure 15. Schematic sketch depicting the formation of progenetic, synthetic, and epigenetic deposits corresponding to different stages of crater formation (*Modified after* Schmieder & Kring [10], James et al. [76]).

The Sudbury crater in Canada represents the world's most economically significant example of melt-dominated syngenetic mineralization [126]. Differentiation of the Sudbury Igneous Complex led to the segregation of dense sulfide liquids enriched in Ni, Cu, Co, and PGE, which accumulated along the base of the melt sheet and in embayments along the crater floor [126]. Although shock processes initially redistributed metals, the extraordinary scale and economic importance of the Sudbury deposits are primarily a consequence of the evolution of the impact melt sheet [13]. Impact melt sheets vary widely in composition depending on the nature of the target rocks, ranging from mafic to felsic and carbonate-rich systems [12]. Even in craters where melt bodies are smaller or discontinuous, melt-breccia interactions can strongly influence subsequent hydrothermal systems by supplying heat, metals, and chemically reactive substrates [3].

Epigenetic mineralization: Post-impact hydrothermal, sedimentary, and hydrocarbon systems

Epigenetic mineralization encompasses deposits formed after crater formation, resulting from prolonged thermal, hydrological, and sedimentary processes within the impact-modified crust [13]. These deposits originate from the crater morphology and thermal inheritance rather than from instantaneous shock-induced mechanical disintegration or melt generation [3].

11.13. Impact-generated Hydrothermal Systems

As impact structures cool, heat retained in melt sheets and uplifted basement rocks drives hydrothermal circulation through fractured crater floors, central uplifts, and ring faults [3], which also aids mineralization. These hydrothermal systems can persist for thousands to hundreds of thousands of years, and in large craters like Chicxulub, potentially longer than a million years. These deposits are coeval with crater formation and represent the most diagnostic mineral systems uniquely attributable to hypervelocity impacts [76]. Hydrothermal alteration produces a wide range of mineral assemblages, including silica, carbonates, sulfides, clays, zeolites, and evaporitic phases, depending on fluid chemistry, temperature, and target lithologies [3].

The Haughton impact structure in Arctic Canada offers an exemplary case of hydrothermal alteration in a carbonate-dominated target. Here, the circulating fluids precipitated a suite of minerals including calcite, barite, celestine, fluorite, marcasite, and zeolites [3]. These assemblages record a cooling trajectory from high-temperature fluids ($>$200 °C) to low-temperature carbonate and silica deposition ($<$60 °C). Remarkably, Haughton also preserves evidence for hydrocarbon-bearing inclusions within calcite veins, illustrating the capacity of impact structures to heat, mobilize, and redistribute organic matter within sedimentary basins. The Ries crater hosts silica-rich hydrothermal deposits, degassing pipes, and quartz-filled fractures within suevite and melt-bearing breccias.

11.14. Sedimentary, Evaporitic, and Hydrocarbon Deposition in Crater Basins

A distinct suite of mineral deposits arises from sedimentary and evaporitic processes within crater basins. Many small- to medium-sized impact craters, especially those in arid or semi-arid regions, evolve into closed drainage basins where long-term lacustrine sedimentation accumulates salts and evaporites [13]. Craters such as Tswaing in South Africa and Lonar in India contain deposits of trona, halite, alkaline carbonates, and other evaporitic minerals that formed long after the impact event but owe their origin entirely to crater morphology. Since impact structures often produce topographic depressions with restricted hydrology, they create ideal conditions for the long-term concentration of dissolved ions in lake waters [76].

Impact structures located within sedimentary basins may also serve as hydrocarbon reservoirs. Ames, Red Wing, and Tookoonooka craters are examples where porous impact breccias, fractured basement rocks, and annular troughs form excellent reservoir spaces [13]. These are overlain by post-impact sedimentary sequences that act as effective seals, creating traps for petroleum accumulation. In such cases, the impact event generates a highly fractured reservoir geometry; meanwhile, subsequent sedimentation and burial emplace structural and stratigraphic traps conducive to hydrocarbon storage [13, 76]. These processes collectively illustrate how hypervelocity impacts reorganize Earth's crust, linking instantaneous shock effects with prolonged geological evolution and resource formation.

12. Conclusion

Impact cratering is a fundamental geological process that has shaped the surfaces, interiors, and evolutionary trajectories of terrestrial planets since the earliest stages of Solar System formation. On Earth, however, its expression is uniquely obscured by active geological resurfacing. This fundamental contrast between Earth and other planetary bodies places terrestrial impact craters at the intersection of opportunity and limitation: while Earth offers unparalleled access to *in situ* observations, laboratory analyses, and subsurface data, its dynamic crust continuously erases or modifies the very structures that record impact history. Consequently, the study of terrestrial impact craters demands a level of diagnostic rigor and interdisciplinary integration that exceeds that required for airless or tectonically inactive bodies.

This review demonstrates that impact cratering is not a singular geological phenomenon but a complex process with cascading consequences across physical, chemical, and biological systems. From shock metamorphism and melt generation to long-lived hydrothermal circulation and crustal reworking, impacts operate far beyond the moment of collision. Their products preserve information about target lithology, impactor composition, and planetary conditions at the time of formation, making terrestrial craters critical archives of Earth's early environment and Solar

System evolution. At planetary scales, impacts have played a central role in regolith formation, formation/destruction of satellites, and other planetary bodies, and also act as the primary chronometers for establishing relative and absolute ages of planetary surfaces across the Solar System.

Beyond their geological significance, impact cratering has profound implications for understanding the evolution of life and planetary habitability, as large impacts have influenced Earth's biosphere through mass extinction events, climate perturbations, and environmental restructuring. At the same time, the degradation and preservation history of craters provides critical insight into Earth's surface evolution and the biases inherent in the terrestrial impact record. These considerations are essential for interpreting crater populations, constraining the temporal evolution of impact flux, and linking terrestrial records with those preserved on more geologically quiescent planetary bodies.

Looking ahead, progress in terrestrial impact research will depend on integrating high-resolution geophysical imaging, advanced microanalytical techniques, improved numerical simulations, and comparative planetology. Reassessment of suspected structures, refinement of diagnostic criteria, and tighter coupling of terrestrial and extraterrestrial datasets remain critical needs of the hour. As planetary exploration continues to expand and sample return missions provide new constraints, terrestrial impact craters will remain indispensable benchmarks for interpreting impact processes across the Solar System.

Thus, impact cratering serves not only as a record of past collisions but also as a fundamental process for investigating planetary evolution, providing a critical link between Earth's geological history and the broader dynamical evolution of the Solar System.

Supplementary Material

Crater Inventory containing the list of known impact structures on Earth, respective coordinates, crater diameter, crater types, age, extent of crater exposure, target type, shock markers, ejecta, and known aftereffects. The inventory is modified after Kenkmann [22], Osinski et al [3], and the Earth Impact Database [23]. The supporting information can be downloaded at: https://doi.org/10.63335/j.hp.2026.0037.

Author contributions

S.S. (Sachana Sathyan): Formal analysis, Methodology, Software, Writing—original draft. S.M. (Sadeeda Marjan): Methodology, Software, Writing—original draft. A.N.: Formal analysis, Methodology, Resources, Writing—original draft. S.M. (Shefana Mahin): Formal analysis, Methodology, Software, Writing—original draft. V.R.R.: Formal analysis, Methodology, Resources, Writing—original draft. S.S. (Sangeeth Sundaresan): Methodology, Resources, Writing—original draft. P.S.: Formal analysis, Methodology, Software, Writing—original draft. S.J.: Formal analysis, Validation, Writing—original draft. J.A.: Methodology, Validation, Writing—original draft. S.R.C.: Methodology, Validation, Writing—original draft. S.K.: Resources, Validation, Writing—original draft. G.K.I.: Methodology, Resources, Validation, Writing—original draft. V.A.: Resources, Validation, Writing—original draft. K.S.S.: Conception, Funding acquisition, Investigation, Project administration, Supervision, Writing—review & editing.

Funding

Department of Science and Technology, Fund for Improvement of Science & Technology (DST-FIST), Government of India, SR/FST/ES-1/2022/109. Anusandhan National Research Foundation (ANRF), SUR/2022/000399. Indian Space Research Organization, DS_2B-13013(2)/16/2022-Sec.2 for funding this project.

Institutional Review Board Statement

Not applicable.

Informed Consent Statement

Not applicable.

Data Availability Statement

Data used in this paper are available from the author upon request.

Acknowledgements

The authors thank the Editor-in-Chief and two anonymous reviewers for providing constructive feedback, which substantially improved the quality of this paper. The entire work was carried out at the Laboratory for Earth Resources Information System (LERIS) housed at the Department of Geology, University of Kerala. LERIS is a collaborative initiative of the Indian Space Research Organization and the University of Kerala.

Conflicts of Interest

The author declares that they have no known competing financial interests or personal relationships that could have influenced the work reported in this paper.

Use of AI and AI-Assisted Technologies

No AI tools were utilized for this paper.

References

1. Melosh, H.J. The physics of very large landslides. *Acta Mech.* **1986**, *64*, 89–99. https://doi.org/10.1007/bf01180100
2. French, B.M. *Traces of Catastrophe: A Handbook of Shock-Metamorphic Effects in Terrestrial Meteorite Impact Structures*; LPI Contribution No. 954; Lunar and Planetary Institute: Houston, TX, USA, 1998; p. 120.
3. Osinski, G.R.; Grieve, R.A.; Ferriére, L.; et al. Impact earth: A review of the terrestrial impact record. *Earth-Sci. Rev.* **2022**, *232*,

104112. 10.1016/j.earscirev.2022.104112

4. Tagle, R.; Schmitt, R.T.; Erzinger, J. Identification of the projectile component in the impact structures Rochechouart, France and Sääksjärvi, Finland: Implications for the impactor population for the earth. *Geochim. Cosmochim. Acta* **2009**, *73*, 4891–4906. https://doi.org/10.1016/j.gca.2009.05.044
5. Ormö, J.; Lindström, M. When a cosmic impact strikes the sea bed. *Geol. Mag.* **2000**, *137*, 67–80. https://doi.org/10.1017/S0016756800003538
6. Alvarez, L.W.; Alvarez, W.; Asaro, F.; et al. Extraterrestrial cause for the Cretaceous-Tertiary extinction. *Science* **1980**, *208*, 1095–1108. https://doi.org/10.1126/science.208.4448.1095
7. French, B.M.; Koeberl, C. The convincing identification of terrestrial meteorite impact structures: What works, what doesn't, and why. *Earth-Sci. Rev.* **2010**, *98*, 123–170. https://doi.org/10.1016/j.earscirev.2009.10.009
8. Barringer, D.M. Coon Mountain and its crater. *Proc. Acad. Nat. Sci. Phila.* **1905**, *57*, 861–886.
9. Dietz, R.S. Vredefort ring structure: meteorite impact scar? *J. Geol.* **1961**, *69*, 499–516. https://doi.org/10.1086/626768
10. Shoemaker, E.M. *Impact mechanics at Meteor Crater*; Princeton University: Princeton, NJ, USA, 1960. https://doi.org/10.3133/ofr59108
11. Schmieder, M.; Kring, D.A. Earth's impact events through geologic time: A list of recommended ages for terrestrial impact structures and deposits. *Astrobiology* **2020**, *20*, 91–141. https://doi.org/10.1089/ast.2019.2085
12. Grieve, R.A.F.; Masaitis, V.L. The economic potential of terrestrial impact craters. *Int. Geol. Rev.* **1994**, *36*, 105–151. https://doi.org/10.1080/00206819409465452
13. Grieve, R. Economic natural resource deposits at terrestrial impact structures. *Geol. Soc. Spec. Publ.* **2005**, *248*, 1e29. https://doi.org/10.1144/GSL.SP.2005.248.01.01
14. Kring, D.A.; Melosh, H.J.; Hunten, D.M. Impact-induced perturbations of atmospheric sulfur. *Earth Planet. Sci. Lett.* **1996**, *140*, 201–212. https://doi.org/10.1016/0012-821X(96)00050-7
15. Hansen, V.L. Geologic mapping of tectonic planets. *Earth Planet. Sci. Lett.* **2000**, *176*, 527–542. https://doi.org/10.1016/S0012-821X(00)00017-0
16. Aswathi, J.; James, S.; Keerthy, S.; et al. Spatio-temporal interpolation of $\sim$ 530 Ma paleo-DEM to quantify denudation of a terrestrial impact crater. *Geomorphology* **2025**, *474*, 109644. https://doi.org/10.1016/j.geomorph.2025.109644
17. Pieters, C.M.; Noble, S.K. Space weathering on airless bodies. *J. Geophys. Res. Planets* **2016**, *121*, 1865–1884. https://doi.org/10.1002/2016JE005128
18. Morgan, J.V.; Gulick, S.P.; Bralower, T.; et al. The formation of peak rings in large impact craters. *Science* **2016**, *354*, 878–882. https://doi.org/10.1126/science.aah6561
19. Ivanov, B.A. Numerical modeling of the largest terrestrial meteorite craters. *Sol. Syst. Res.* **2005**, *39*, 381–409. https://doi.org/10.1007/s11208-005-0051-0
20. Gomes, R.; Levison, H.; Tsiganis, K.; et al. Origin of the cataclysmic Late Heavy Bombardment period of the terrestrial planets. *Nature* **2005**, *435*, 466–469. https://doi.org/10.1038/nature03676
21. Morgan, J.W. and Wandless, G.A. Strangways Crater, Northern Territory, Australia: Siderophile element enrichment and lithophile element fractionation. *J. Geophys. Res. Solid Earth* **1983**, *88*, A819–A829. https://doi.org/10.1029/JB088iS02p0A819
22. Kenkmann, T. The terrestrial impact crater record: A statistical analysis of morphologies, structures, ages, lithologies, and more. *Meteorit. Planet. Sci.* **2021**, *56*, 1024–1070. https://doi.org/10.1111/maps.13657
23. Planetary and Space Science Centre. *Earth Impact Database*; University of New Brunswick: Fredericton, New Brunswick, Canada, 2020. http://www.passc.net/EarthImpactDatabase/Newwebsite_05-2018/Index.html
24. Osinski, G.R.; Cockell, C.S.; Pontefract, A.; et al. The role of meteorite impacts in the origin of life. *Astrobiology* **2020**, *20*, 1121–1149. https://doi.org/10.1089/ast.2019.2203
25. Reimold, W.U.; Koeberl, C. Impact structures in Africa: A review. *J. Afr. Earth Sci.* **2014**, *93*, 57–175. https://doi.org/10.1016/j.jafrearsci.2014.01.008
26. Ivanov, B.A.; Neukum, G.; Bottke, W.; et al. The comparison of size frequency distributions of impact craters and asteroids and the planetary cratering rate. In *Asteroids III*; Bottke, W., Cellino, P., Paolicchi, P., Binzel, R.P., Eds.; University of Arizona Press: Tucson, AZ, USA, 2003; pp. 89–101. https://doi.org/10.2307/j.ctv1v7zdn4.13
27. Becker, L.; Poreda, R.J.; Basu, A.R.; et al. A possible end-Permian impact crater offshore of northwestern Australia. *Science* **2004**, *304*, 1469–1476. https://doi.org/10.1126/science.1093925
28. Montanari, A.; Koeberl, C. *Impact Stratigraphy: The Italian Record*; Lecture Notes in Earth Sciences 93; Springer-Verlag: Heidelberg, Germany, 2000; p. 364.
29. Koeberl, C.; Claeys, P.; Hecht, L.; et al. Geochemistry of impactites. *Elements* **2012**, *8*, 37–42. https://doi.org/10.2113/gselements.8.1.37
30. Moser, D.E.; Cupelli, C.L.; Barker, I.R.; et al. New zircon shock phenomena and their use for dating and reconstruction of large impact structures revealed by electron nanobeam (BSD, CL, EDS) and isotopic U–Pb and (U–Th)/He analysis on the Vredefort Dome. *Can. J. Earth Sci.* **2011**, *48*, 117–139. https://doi.org/10.1139/e11-011
31. Hörz, F. Statistical measurements of deformation structures and refractive indices in experimentally shock-loaded quartz. *J. Geophys. Res.* **1968**, *73*, 6019–6038. https://doi.org/10.1029/JB073i018p06019
32. Goltrant, O.; Leroux, H.; Doukhan, J-C.; et al. Formation mechanisms of planar deformation features in naturally shocked quartz. *Phys. Earth Planet. Inter.* **1992**, *74*, 219–240. https://doi.org/10.1016/0031-9201(92)90012-K
33. Kumar, P.S.; Head, J.W.; Kring, D.A. Erosional modification and gully formation at Meteor Crater, Arizona: Insights into crater degradation processes on Mars. *Icarus* **2010**, *208*, 608–620. https://doi.org/10.1016/j.icarus.2010.03.032
34. Ferriére, L.; Koeberl, C.; Brandstätter, F.; et al. Geochemistry of basement rocks and impact breccias from the central uplift of the Bosumtwi crater, Ghana—Comparison of proximal and distal impactites. In: *Large Meteorite Impacts and Planetary Evolution IV*; Geological Society of America Special Paper, Volume 465; Geological Society of America: Boulder. CO, USA, 2010. https://doi.org/10.1130/2010.2465(22)
35. Ferrière1, L.; Koeberl, C.; Reimold, W.U.; et al. Ballen quartz and cristobalite in impact breccias: Types, occurrence, and possible origin. In *Large Meteorite Impacts and Planetary Evolution IV*; LPI Contribution No. 1423; Lunar and Planetary Institute: Houston, TX, USA, 2008. (Abstract #3011)
36. Ferrière, L.; Koeberl, C.; Reimold, W.U. Characterization of ballen quartz and cristobalite in impact breccias: New observations and constraints on ballen formation. *Eur. J. Mineral.* **2009**, *21*, 203–217. https://doi.org/10.1127/0935-1221/2009/0021-1898
37. Tsikalas, F.; Faleide, J.I.; Werner, S.C.; et al. The Mølnir impact event and its consequences. In *Geology and Geophysics of a Late Jurassic/Early Cretaceous Marine Impact Event*; Tsikalas, F., Dypvik, H., Smelror, M., Eds.; Geological Society of London: London, UK, 2010; pp. 75–137.
38. Dressler, B.O.; Crabtree, D.; Schuraytz, B.C. Incipient melt formation and devitrification at the Wanapitei impact structure, Ontario, Canada. *Meteorit. Planet. Sci.* **1997**, *32*, 249–258. https://doi.org/10.1111/J.1945-5100.1997.TB01263.X
39. Palme, H.; Janssens, M.J.; Takahashi, H.; et al. Meteoritic material

at five large impact craters. *Geochim. Cosmochim. Acta* **1978**, *42*, 313–323. https://doi.org/10.1016/0016-7037(78)90184-9

40. Whitehead, J.; Grieve, R.A.F.; Spray, G. Mineralogy and petrology of melt rocks from the Popigai impact structure, Siberia. *Meteorit. Planet. Sci.* **2002**, *37*, 623–647. http://dx.doi.org/10.1111/j.1945-5100.2002.tb00844.x
41. Koeberl, C.; Holland, H.D.; Turekian, K.K. The geochemistry and cosmochemistry of impacts. In *Radioactive Geochronometry from the Treatise on Geochemistry*; Elsevier: Oxford, UK, 2014; pp. 73–118. https://doi.org/10.1016/B978-008043751-4/00228-5
42. Koeberl, C. Mineralogical and geochemical aspects of impact craters. *Mineral. Mag.* **2002**, *66*, 745–768. https://doi.org/10.1180/0026461026650059
43. Koeberl, C.; Reimold, W.U.; Cooper, G.; et al. Aorounga and Gweni Fada impact structures, Chad: Remote sensing, petrography, and geochemistry of target rocks. *Meteorit. Planet. Sci.* **2005**, *40*, 1455–1471. http://dx.doi.org/10.1111/j.1945-5100.2005.tb00412.x
44. O'Brien, D.P.; Izidoro, A.; Jacobson, S.A.; et al. The delivery of water during terrestrial planet formation. *Space Sci. Rev.* **2018**, *214*, 47. https://doi.org/10.1007/s11214-018-0475-8
45. Gilmour, I.; French, B.M.; Franchi, I.A.; et al. Geochemistry of carbonaceous impactites from the Gardnos impact structure, Norway. *Geochim. Cosmochim. Acta* **2003**, *67*, 3889–3903. https://doi.org/10.1016/S0016-7037(03)00213-8
46. Chandran, S.R.; James, S.; Santosh, M.; et al. Geochemical and geochronological evidence of meteorite impact excavating the Archean basement at Lonar Crater, Central India. *Lithos* **2021**, *404*, 106479. https://doi.org/10.1016/j.lithos.2021.106479
47. Chen, M.; Koeberl, C.; Xiao, W.; et al. Planar deformation features in quartz from impact-produced polymict breccia of the Xiuyan crater, China. *Meteorit. Planet. Sci.* **2011**, *46*, 729–736. https://doi.org/10.1111/j.1945-5100.2011.01186.x
48. Palme, H.; Grieve, R.A.; Wolf, R. Identification of the projectile at the Brent crater, and further considerations of projectile types at terrestrial craters. *Geochim. Cosmochim. Acta* **1981**, *45*, 2417–2424. https://doi.org/10.1016/0016-7037(81)90095-8
49. Pati, J.K.; Reimold, W.U.; Koeberl, C.; et al. The Dhala structure, bhundelkand craton, Central India-eroded remnant of a large Paleoproterozoic impact structure. *Meteorit. Planet. Sci.* **2008**, *43*, 1383–1398. http://dx.doi.org/10.1111/j.1945-5100.2008.tb00704.x
50. McDonald, I.; Andreoli, M.A.G.; Hart, R.J.; et al. Platinum-group elements in the Morokweng impact structure, South Africa: Evidence for the impact of a large ordinary chondrite projectile at the Jurassic-Cretaceous boundary. *Geochim. Cosmochim. Acta* **2001**, *65*, 299–309. https://doi.org/10.1016/S0016-7037(00)00527-5
51. McDonough, W.F.; Sun, S.S. The composition of the Earth. *Chem. Geol.* **1995**, *120*, 223–253. https://doi.org/10.1016/0009-2541(94)00140-4
52. Anders, E.; Grevesse, N. Abundances of the elements: Meteoritic and solar. *Geochim. Cosmochim. Acta* **1989**, *53*, 197–214. https://doi.org/10.1016/0016-7037(89)90286-X
53. Tagle, R.; Erzinger, J.; Hecht, L.; et al. Platinum group elements in impactites of the ICDP Chicxulub drill core Yaxcopoil-1: Are there traces of the projectile? *Meteorit. Planet. Sci.* **2004**, *39*, 1009–1016. https://doi.org/10.1111/j.1945-5100.2004.tb00942.x
54. Tagle, R.; Claeys, P. An ordinary chondrite impactor for the Popigai crater, Siberia. *Geochim. Cosmochim. Acta* **2005**, *69*, 2877–2889. https://doi.org/10.1016/j.gca.2004.11.024
55. Sturkell, E.F.; Ormö, J. Magnetometry of the marine, Ordovician Lockne impact structure, Jämtland, Sweden. *J. Appl. Geophys.* **1998**, *38*, 195–207. https://doi.org/10.1016/S0926-9851(97)00031-1
56. Masaitis, V.L. The middle Devonian Kaluga impact crater (Russia): New interpretation of marine setting. *Deep-Sea Res. Part II Top. Stud. Oceanogr.* **2002**, *49*, 1157–1169. https://doi.org/10.1016/S0967-0645(01)00142-4
57. Milne, D.H.; McKay, C.P. Response of marine plankton communities to a global atmospheric darkening. In *Geological Implications of Impacts of Large Asteroids and Comets on the Earth*; Silver, L.T., Schultz, P.H., Eds.; GSA: Boulder, CO, USA, 1982.
58. Sajinkumar, K.S.; James, S.; Indu, G.K.; et al. The Luna structure, India: A probable impact crater formed by an iron bolide. *Planet. Space Sci.* **2024**, *240*, 105826. https://doi.org/10.1016/j.pss.2023.105826
59. Goderis, S.; Kalleson, E.; Tagle, R.; et al. A non-magmatic iron projectile for the Gardnos impact event. *Chem. Geol.* **2009**, *258*, 145–156. https://doi.org/10.1016/j.chemgeo.2008.09.025
60. Mittlefehldt, D.W.; Hörz, F.; See, T.H.; et al. Geochemistry of target rocks, impact-melt particles, and metallic spherules from Meteor Crater, Arizona: Empirical evidence on the impact process. In *Large Meteorite Impacts III*; Kenkmann, T., Hörz, F., Deutsch, A., Eds.; GSA: Boulder, CO, USA, 2005. https://doi.org/10.1130/0-8137-2384-1.367
61. Gulick, S.P.; Barton, P.J.; Christeson, G.L.; et al. Importance of pre-impact crustal structure for the asymmetry of the Chicxulub impact crater. *Nat. Geosci.* **2008**, *1*, 131–135. https://doi.org/10.1038/ngeo103
62. Deutsch, A.; Lakomy, R.; Buhl, D. Strontium- and neodymium-isotopic characteristics of a heterolithic breccia in the basement of the Sudbury impact structure, Canada. *Earth Planet. Sci. Lett.* **1989**, *93*, 359–370. https://doi.org/10.1016/0012-821X(89)90035-6
63. Walker, R.J.; Morgan, J.W.; Naldrett, A.J.; et al. Re-Os isotope systematics of Ni-Cu sulfide ores, Sudbury Igneous Complex, Ontario: Evidence for a major crustal component. *Earth Planet. Sci. Lett.* **1991**, *105*, 416–429. https://doi.org/10.1016/0012-821X(91)90182-H
64. Trinquier, A.; Birck, J.L.; Allègre, C.J. The nature of the KT impactor. A 54Cr reappraisal. *Earth Planet. Sci. Lett.* **2006**, *241*, pp. 780–788. https://doi.org/10.1016/j.epsl.2005.11.006
65. Hodych, J.P.; Dunning, G.R. Did the Manicouagan impact trigger end-of-Triassic mass extinction? *Geology* **1992**, *20*, 51–54. https://doi.org/10.1016/j.epsl.2005.11.006
66. Koeberl, C.; Shirey, S.B. Detection of a meteoritic component in Ivory Coast tektites with rhenium-osmium isotopes. *Science* **1993**, *261*, 595–598. https://doi.org/10.1126/science.261.5121.595
67. Koeberl, C.; Shirey, S.B. Re–Os isotope systematics as a diagnostic tool for the study of impact craters and distal ejecta. *Palaeogeogr. Palaeoclimatol. Palaeoecol.* **1997**, *132*, 25–46. https://doi.org/10.1016/S0031-0182(97)00045-X
68. Tagle, R.; Hecht, L. Geochemical identification of projectiles in impact rocks. *Meteorit. Planet. Sci.* **2006**, *41*, 1721–1735. https://doi.org/10.1111/j.1945-5100.2006.tb00448.x
69. Kyte, F.T.; Shukolyukov, A.; Lugmair, G.W.; et al. Early Archean spherule beds: Chromium isotopes confirm origin through multiple impacts of projectiles of carbonaceous chondrite type. *Geology* **2003**, *31*, 283–286. https://doi.org/10.1130/0091-7613(2003)031%3C0283:EASBCI%3E2.0.CO;2
70. Lugmair, G.W.; Shukolyukov, A. Early solar system timescales according to 53Mn-53Cr systematics. *Geochim. Cosmochim. Acta* **1998**, *62*, 2863–2886. https://doi.org/10.1016/S0016-7037(98)00189-6
71. Artemieva, N.; Morgan, J. Global K-Pg layer deposited from a dust cloud. *Geophys. Res. Lett.* **2020**, *47*, e2019GL086562. https://doi.org/10.1029/2019GL086562
72. Meier, R.; Owen, T.C.; Matthews, H.E.; et al. A determination of the HDO/H_2O ratio in Comet C/1995 O1 (Hale-Bopp). *Science* **1998**, *279*, 842–844. https://doi.org/10.1126/science.279.5352.842
73. O'Neill, C.; Marchi, S.; Bottke, W.; et al. The role of impacts on Archaean tectonics. *Geology* **2020**, *48*, 174–178. https://doi.org/10.1130/G46533.1
74. Pernicka, E.; Kaether, D.; Koeberl, C. Siderophile element concentrations in drill core samples from the Manson crater. In *The Man-*

son Impact Structure, Iowa; Anatomy of an Impact Crater; Koeberl, C., Anderson, R.R., Eds.; Geological Society of America: Boulder, CO, USA, 1996. https://doi.org/10.1130/0-8137-2302-7.325

75. Arens, N.C.; Jahren, A.H. Carbon isotope excursion in atmospheric CO_2 at the Cretaceous-Tertiary boundary: Evidence from terrestrial sediments. *Palaios* **2000**, *15*, 314–322. https://doi.org/10.2307/3515539
76. James, S.; Chandran, S.R.; Santosh, M.; et al. Meteorite impact craters as hotspots for mineral resources and energy fuels: A global review. *Energy Geosci.* **2022**, *3*, 136–146. https://doi.org/10.1016/j.engeos.2021.12.006
77. Luck, J.M.; Turekian, K.K. Osmium-187/Osmium-186 in manganese nodules and the Cretaceous-Tertiary boundary. *Science* **1983**, *222*, 613–615. https://doi.org/10.1126/science.222.4624.613
78. Kring, D.A. The Chicxulub impact event and its environmental consequences at the Cretaceous–Tertiary boundary. *Palaeogeogr. Palaeoclimatol. Palaeoecol.* **2007**, *255*, 4–21. https://doi.org/10.1016/j.palaeo.2007.02.037
79. Indu, G.K.; James, S.; Chandran, S.R.; et al. Deriving a denudation index for terrestrial meteorite impact craters using drainages as proxies. *Geomorphology* **2022**, 397, 108007. *http://doi.org/10.1016/j.geomorph.2021.108007*
80. Neukum, G. Meteoritenbombardement und datierung planetarer oberflachen. Habilitation Dissertation for Faculty Membership, Ludwig-Maximilians-Univ, Munich, Germany, 1983.
81. Trigo-Rodríguez, J.M. Craters and Extinctions in the Geological Record. In *Asteroid Impact Risk: Impact Hazard from Asteroids and Comets*; Springer International Publishing: Cham, Switzerland, 2022; pp. 107–126. https://doi.org/10.1007/978-3-030-95124-5_6
82. Platz, T.; Michael, G.G.; Neukum, G. Confident thickness estimates for planetary surface deposits from concealed crater populations. *Earth Planet. Sci. Lett.* **2010**, *293*, 388–395. https://doi.org/10.1111/maps.12924
83. Marty, B. Meteoritic noble gas constraints on the origin of terrestrial volatiles. *Icarus* **2022**, *381*, 115020. https://doi.org/10.1016/j.icarus.2022.115020
84. Milne, D. H.; McKay, C.P. Response of marine plankton communities to a global atmospheric darkening. In *Geological Implications of Impacts of Large Asteroids and Comets on the Earth*; Silver, L.T., Schultz, P.H. Eds.; GSA: Boulder, CO, USA, 1982.
85. Nandakumar, A.; Mohan, S.; Sathyan, S.; et al. Crater Ray Explorer (CRAYEX): Toolkit to evaluate the spallation expanse of rayed craters on lunar surface. *Meteorit. Planet. Sci.* **2026**, 61, 300–312. https://doi.org/10.1111/maps
86. Hiral, P.B.; Anbazhagan, S.; Rahul, S.; et al. Reconstructing the geological and geomorphological history of Morella Crater, Mars. *Geomorphology* **2025**, *479*, 109740. https://doi.org/10.1016/j.geomorph.2025.109740
87. Rampino, M.R. Relationship between impact-crater size and severity of related extinction episodes. *Earth-Sci. Rev.* **2020**, *201*, 102990. https://doi.org/10.1016/j.earscirev.2019.102990
88. Chapman, C.R. The hazard of near-Earth asteroid impacts on earth. *Earth Planet. Sci. Lett.* **2004**, *222*, 1–15. https://doi.org/10.1016/j.epsl.2004.03.004
89. Canup, R.M.; Righter, K. *Origin of the Earth and Moon*; University of Arizona Press: Tucson, AZ, USA, 2000; Volume 30.
90. Pieters, C.M.; Taylor, L.A.; Noble, S.K.; et al. Space weathering on airless bodies: Resolving a mystery with lunar samples. *Meteorit. Planet. Sci.* **2000**, *35*, 1101–1107. https://doi.org/10.1002/2016JE005128
91. Chapman, C.R. Space weathering of asteroid surfaces. *Annu. Rev. Earth Planet. Sci.* **2004**, *32*, 539–567. https://doi.org/10.1146/annurev.earth.32.101802.120453
92. Hartung, J.B.; Horz, F.; Gault, D.E. The origin and significance of lunar microcraters. In *Abstracts of the Lunar and Planetary Science Conference*; Lunar and Planetary Science Institute: Houston, TX, USA, 1972; Volume 3, p. 363.
93. Pierazzo, E.; Hahmann, A.N.; Sloan, L.C. Chicxulub and climate: Radiative perturbations of impact-produced S-bearing gases. *Astrobiology* **2003**, *3*, 99–118. https://doi.org/10.1089/153110703321632453
94. Deutsch, A.N.; Neumann, G.A.; Kreslavsky, M.A.; et al. Temperature-related variations of 1064 nm surface reflectance on mercury: Implications for space weathering. *Planet. Sci. J.* **2024**, *5*, 8. https://doi.org/10.3847/PSJ/ad0e6d
95. Shoemaker, E.M. *Impact mechanics at Meteor Crater, Arizona*; Princeton University: Princeton, NJ, USA, 1960. https://doi.org/10.3133/ofr59108
96. Keller, L.P.; Thompson, M.S.; Seifert, L.B.; et al. Space weathering effects in Bennu asteroid samples. *Nat. Geosci.* **2025**, *18*, 825–831. https://doi.org/10.1038/s41561-025-01745-w
97. Hartmann, W.K. Martian cratering 8. Isochron refinement and the history of Martian geologic activity. *Icarus* **2005**, *174*, 294–320. https://doi.org/10.1016/j.icarus.2004.11.023
98. Neish, C.D.; Molaro, J.L.; Lora, J.M.; et al. Fluvial erosion as a mechanism for crater modification on Titan. *Icarus* **2016**, *270*, 114–129. https://doi.org/10.1016/j.icarus.2015.07.022
99. Fassett, C.I.; Kadish, S.J.; Head, J.W.; et al. The global population of large craters on Mercury and comparison with the Moon. *Geophys. Res. Lett.* **2011**, *38*, L10201. https://doi.org/10.1029/2011GL047294
100. Bougher, S.W., Hunten, D.M., Phillips, R.J., Eds.; *Venus II: Geology, Geophysics, Atmosphere, and Solar wind Environment*; University of Arizona Press: Tucson, AZ, USA, 2022.
101. Robertson, P.B. Zones of shock metamorphism at the Charlevoix impact structure, Quebec. *Bull. Geol. Soc. Am.* **1975**, *86*, 1630–1638. https://doi.org/10.1130/0016-7606(1975)86<1630:ZOSMAT>2.0.CO;2
102. Hiesinger, H.; Marchi, S.; Schmedemann, N.; et al. Cratering on Ceres: Implications for its crust and evolution. *Science* **2016**, *353*, aaf4759. https://doi.org/10.1126/science.aaf4759
103. Pike, R.J. Control of crater morphology by gravity and target type. In *Proceedings of the 11th Lunar and Planetary Science Conference*; Lunar and Planetary Institute (LPI): Houston, TX, USA, 1980; pp. 2159–2189.
104. Poulet, F.; Cruikshank, D.P.; Cuzzi, J.N.; et al. Compositions of Saturn's rings A, B, and C from high-resolution near-infrared spectroscopic observations. *Astron. Astrophys.* **2003**, *412*, 305–316. https://doi.org/10.1051/0004-6361:20031123
105. Melosh, H.J.; Schneider, N.M.; Zahnle, K.J.; et al. Ignition of global wildfires at the Cretaceous/Tertiary boundary. *Nature* **1990**, *343*, 251–254. https://doi.org/10.1038/343251a0
106. Mittlefehldt, D.W.; See, T.H.; Hörz, F. Dissemination and fractionation of projectile materials in the impact melts from Wabar Crater, Saudi Arabia. *Meteoritics* **1992**, *27*, 361–370. https://doi.org/10.1111/j.1945-5100.1992.tb00217.x
107. Fortezzo, C.M.; Spudis, P.D.; Harrel, S.L. *Unified Geologic Map of the Moon*; U.S. Geological Survey: Reston, VA, USA, 2020.
108. Nicholson, U.; Powell, W.; Gulick, S.; et al. 3D anatomy of the Cretaceous–Paleogene age Nadir Crater. *Commun. Earth Environ.* **2024**, *5*, 547. https://doi.org/10.21203/rs.3.rs-4363378/v1
109. Poag, C.W.; Plescia, J.B.; Molzer, P.C. Ancient impact structures on modern continental shelves: The Chesapeake Bay, Montagnais, and Toms Canyon craters, Atlantic margin of North America. *Deep-Sea Res. II Top. Stud. Oceanogr.* **2002**, *49*, 1081–1102. https://doi.org/10.1016/S0967-0645(01)00144-8
110. Canup, R.M. A giant impact origin of Pluto-Charon. *Science* **2005**, *307*, 546–550. https://doi.org/10.1126/science.1106818
111. Cuzzi, J.N.; Estrada, P.R. Compositional evolution of Saturn's rings due to meteoroid bombardment. *Icarus* **1998**, *132*, 1–35. https://doi.org/10.1006/icar.1997.5863

112. Bussmann, M.; Reinhardt, C.; Gillmann, C.; et al. The possibility of a giant impact on Venus (accepted). *Astron. Astrophys.* **2025**, 702, A106. https://doi.org/10.1051/0004-6361/202555802

113. Coleman, E.; Nottingham, T.; Robinson, S.; et al. Explaining Venus' retrograde rotation. *Phys. Spec. Top.* **2018**, *17*, 1–4.

114. Chatterjee, S.; Yadav, S. The origin of the prebiotic information system in the peptide/RNA world: A simulation model of the evolution of translation and the genetic code. *Life* **2019**, *9*, 25. https://doi.org/10.3390/life9010025

115. Osinski, G.R.; Tornabene, L.L.; Banerjee, N.R.; et al. Impact-generated hydrothermal systems on Earth and Mars. *Icarus* **2013**, *224*, 347–363. https://doi.org/10.1016/j.icarus.2012.08.030

116. Mangold, N.; Adeli, S.; Conway, S.; et al. A chronology of early Mars climatic evolution from impact crater degradation. *J. Geophys. Res. Planets* **2012**, *117*, E04003. https://doi.org/110.1029/2011JE004005

117. Hallis, L.J. D/H ratios of the inner Solar System. *Philos. Trans. R. Soc. A* **2017**, *375*, 20150390. https://doi.org/10.1098/rsta.2015.0390

118. McDonough, W.F.; Sun, S.S. The composition of the Earth. *Chem. Geol.* **1995**, *120*, 223–253. https://doi.org/10.1016/0009-2541(94)00140-4

119. Lightfoot, P.C. *Nickel Sulfide Ores and Impact Melts: Origin of the Sudbury Igneous Complex*; Elsevier Inc.: Amsterdam, The Netherlands, 2017.

120. Cordiner, M.A.; Roth, N.X.; Kelley, M.S.P.; et al. JWST detection of a carbon dioxide dominated gas coma surrounding interstellar object 3I/ATLAS. *Astrophys. J. Lett.* **2025**, *991*, L43. https://doi.org/10.48550/arXiv.2508.18209

121. Bond, D.P.; Grasby, S.E. On the causes of mass extinctions. *Palaeogeogr. Palaeoclimatol. Palaeoecol.* **2017**, *478*, 3–29. https://doi.org/10.1016/j.palaeo.2016.11.005

122. Racki, G. Big 5 mass extinctions. In *Encyclopedia of Geology*; Elsevier: Oxford, UK, 2021.

123. Longrich, N.R.; Tokaryk, T.; Field, D.J. Mass extinction of birds at the Cretaceous–Paleogene (K–Pg) boundary. *Proc. Natl. Acad. Sci. USA* **2011**, *108*, 15253–15257. https://doi.org/10.1073/pnas.1110395108

124. Milne, D.H.; McKay, C.P. *Response of Marine Plankton Communities to a Global Atmospheric Darkening*; National Aeronautics and Space Administration: Washington, DC, USA, 1982.

125. Kaiho, K.; Oshima, N.; Adachi, K.; et al. Global climate change driven by soot at the K-Pg boundary as the cause of the mass extinction. *Sci. Rep.* **2016**, *6*, 28427. https://doi.org/10.1038/srep28427

126. Li, S.S.; Keerthy, S.; Santosh, M.; et al. Anatomy of impactites and shocked zircon grains from Dhala reveals Paleoproterozoic meteorite impact in the Archean basement rocks of central India. *Gondwana Res.* **2018**, *54*, 81–101. http://doi.org/10.1016/j.gr.2018.03.018